博士論文

Controlling role of soil and groundwater on shallow landslides triggered by earthquakes

LI RAN

平成29年度入学

島根大学大学院総合理工学研究科博士後期課程

総合理工学専攻 地球科学・地球環境 コース

主指導教員: 酒井哲弥

令和 2 年 7 月 10 日

Abstract

Earthquake-triggered landslide is a major secondary disaster following the strong ground motion, especially in the hilly region. The occurrence of the coseismic landslide is concluded to be closely related to the seismic intensity, peak ground acceleration (PGA), topography, geological condition, and groundwater in previous studies. Massive large landslides have been investigated in detail in previous studies for their long runout and high mobilization. However, the research on the coseismic landslides on small scales is relatively insufficient. In this work, the coseismic landslides triggered by the 2018 Eastern Iburi Earthquake and a flow-like landslide triggered by the 2018 Western Shimane Earthquake were selected as the targets to study the influence of the soil behavior and groundwater on the slope failures triggered by the earthquake.

At 03:08 (JST) on September 6, 2018, a M_j 6.7 earthquake struck the Eastern Iburi region of Hokkaido, Northern Japan. More than 5,000 landslides were simultaneously triggered by the strong ground motion. Only two deep-seated landslides were confirmed, and the rest of the Iburi landslides are mainly shallow debris slides. Based on the field reconnaissance, the shallow debris slides were further categorized into three types: steep debris slide, gentle debris slide, and mobilization of V-shaped convergent sliding masses. The three types of shallow landslides were investigated in depth through longitudinal sections, vertical stratigraphic sections, and in-situ hardness tests. All three types of shallow landslides were found to initiate from the liquefied failure of the weak Ta-d pumice layer and further evolve to the overall mobilization of the superimposed pyroclastic fall deposits along the liquefied sliding zone. Also, the positive relationship between coseismic landslide density and Ta-d pumice thickness demonstrates the controlling role of the Ta-d on Iburi landslide occurrence from a macro perspective.

To study the shear behavior as well as the anti-liquefaction strength of the soils around the sliding zone, a series of laboratory tests were conducted. The Ta-d pumice around the sliding zone is subdivided into Ta-d pumice MG (medium gravel), Ta-d pumice FG (fine gravel), Ta-d pumice CS (coarse sand), and Ta-d pumice MS (medium sand) based on the color, particle size,

and particle strength. The results of static consolidated-undrained triaxial compression tests and cyclic triaxial compression tests on Ta-d pumice and paleosol underlying the Ta-d pumice indicate that the medium sandy Ta-d pumice MS and the fragile Ta-d pumice CS have lower shear resistance and anti-liquefaction strength than other layers and can be easily liquefied under intense ground motion. The stable low-permeability paleosol layer underlying the Ta-d pumice enables the seepage flow parallel to the slope and further results in the erosion and weathering of the Ta-d pumice. This explains the extensive existence of the Ta-d pumice MS or fragile Ta-d pumice CS in the landslide distribution area.

At 01:32 (JST) on April 9, 2018, a M 6.1 earthquake struck Oda, Shimane, Japan. Two landslides were triggered by this earthquake. The two landslides are not distributed in the area suffered from the most intense ground motion and the Kataragai landslide occurred in a gentle slope with a slope angle of approximately 7°. The occurrence of the two landslides seems to be controlled more by the geological and hydrological conditions.

It is confirmed through the field survey that the Kataragai landslide occurred in an artificial slope that refilled with the medium sand with gravel. Several small pools were observed on the slope with perennial water. The dry density of the soil decreases to a low value and then increases in the vertical direction. The sliding zone is a medium sandy layer with a low dry density and fine-particle content. The soil strength of the medium sandy layer reaches a low value both in the hardness tests and penetration tests. The results of triaxial tests indicate that the anti-liquefaction strength of the soils in the Kataragai landslide is relatively low on the whole, and the anti-liquefaction strength of the interlayer in the sliding zone is lower than other soil layers. The downslope seepage flow was validated by the self-potential test and the seepage flows at the crown near the pool were more noticeable. The erosion due to the seepage flow can significantly contribute to the formation of weak soil layers.

Through the study on landslides triggered by the Western Shimane earthquake and the Eastern Iburi earthquake, it is found that the weathering and erosion of soil due to the seepage flow can significantly contribute to the formation of the low anti-liquefaction strength soil layer which commonly controls the thickness of the sliding mass and locality of the sliding zone during earthquakes.

Acknowledgement

The thesis entitled "*Controlling role of soil and groundwater on shallow landslides triggered by earthquakes*" is written in order to fulfill the partial requirement for the degree of doctor in the Department of Earth Science, Interdisciplinary Faculty of Science and Engineering, Shimane University, Japan.

First and foremost, I would like to express my deepest appreciation to my enthusiastic supervisor, Professor Fawu Wang, for his continuous guidance, support, and encouragement throughout my Ph.D. study at Shimane University. His immense ideas, suggestions, and patience give me endless power to overcome difficulties confronted during the research. His tremendous knowledge and positive attitude towards life and research will be lifelong benefits for me.

I wish to express my sincere gratitude to all the professors and staff at Shimane University, for their academic support and kind help in my Ph.D. study. I am grateful to all members of my dissertation committee for their time on the review and evaluation during the application. The valuable comments and suggestions from the dissertation committee are of great help to improve the quality of this thesis.

Many thanks to my Ph.D. fellows (Professor Feng Ji, Professor Zili Dai, Mr. Shuai Zhang, Mr. Prakash Dhungana, Mr. Kounghoon Nam, Ms. Rong Zhou, Mr. Yoshiharu Yokota, and Mr. Akinori Iio) for their kind support during this research. The life, the field works, the seminars, and the conferences we shared will be lifelong reminiscence.

Table of contents

List of tables

List of figures

Introduction

1.1 Background

Earthquake-triggered landslide is a major secondary hazard following the strong ground motion, especially in the hilly region (Keefer 1994; Owen et al. 2008; Wang et al. 2009). The damages and social effects resulted from the coseismic landslides even override those directly from the earthquake. The great 1995 Hyogoken-Nambu earthquake (Mw 6.9) induced 674 landslides within an area of about 700 km^2 and was responsible for 6,289 fatalities (Sassa et al. 1996; Fukuoka et al. 1997); the 1999 M_L 7.3 Chi-chi earthquake occurred in the central area of Taiwan, resulted in tens of thousands of landslides and accounted for about 2,400 deaths (Wang et al. 2002); More than 15,000 geohazards were generated during the Ms 8.0 Wenchuan earthquake and claimed about 20,000 deaths (Yin et al. 2009); the 2015 Gorkha earthquake sequence occurred in high-elevation and steep-topography areas and induced thousands of landslides, which killed hundreds of people (Collins and Jibson 2015); in the 2016 Kumamoto earthquake sequence 3,467 coseismic landslides were resulted and 50 people were killed (Xu et al. 2018a); the 2018 M_j 6.7 Hokkaido Eastern Iburi earthquake resulted in more than 5000 landslides within an area of 46.3 km^2 and accounted for 41 deaths. The destructive damage and catastrophic consequence caused by earthquake-triggered landslides have attracted much attention worldwide and earthquake-triggered landslides have been a hot topic in recent decades. To explore the failure mechanism and controlling factors of the earthquake-triggered landslides is of great importance for the disaster prevention and mitigation in this area or this type of landslide.

The occurrence of the coseismic landslide is concluded to be closely related to the seismic intensity, peak ground acceleration (PGA), topography, geological condition, and groundwater in previous studies (Liao and Lee 2000; Wang et al. 2002; Gorum et al. 2013; Xu and Xu 2014; Xu et al. 2015; Zhang et al. 2019a). Massive large landslides, such as the landslides triggered by the

2004 Mid Niigata earthquake in Japan (Chigira and Yagi 2006), the Hattian Bala rock avalanche in Pakistan in 2005 (Dunning et al. 2007), and the Daguangbao landslide in China in 2008 (Huang et al. 2012), have attracted much attention for their destructive consequence and have been investigated in detail in previous studies. However, the research on the coseismic landslides on small scales is relatively insufficient. The 2018 Hokkaido Eastern Iburi earthquake triggered more landslides than other earthquakes with similar magnitude (Zhang 2019b). Two landslides (the Kataragai landslide and the Shitsumi landslide) were triggered in the 2018 Western Shimane Earthquake. The two landslides are not distributed in the area suffered from the most intense ground motion and the Kataragai landslide occurred in a gentle slope with a slope angle of approximately 7°. These phenomena seem to be controlled more by the geological and hydrological conditions.

Many studies concerning the spatial distribution and controlling factors of the Iburi landslides have been conducted. Osanai et al. (2019) introduced the characteristics of coseismic landslides based on of field investigations. Zhang et al. (2019a) and Wang et al. (2019) delineated detailed landslide inventory and analyzed the effect of seismic, topographic, and geological factors on coseismic landslide occurrence and distribution. Shao et al. (2019) performed the learning-based susceptibility mapping based on the established landslide inventory. These articles mostly analyze the characteristics of existing landslides from a macro perspective. However, the controlling role of the soil (especially the shear resistance and liquefaction resistance of the pumice) and groundwater on the Iburi landslide occurrence has not been well studied yet. The two landslides triggered by the 2018 Western Shimane Earthquake did not attract extensive attention. There has not been a detailed study of the characteristics of these two landslides.

In this work, the coseismic landslides triggered by the 2018 Hokkaido Eastern Iburi Earthquake and the Kataragai landslide triggered by the 2018 Western Shimane Earthquake were selected as the targets to study the influence of the soil behavior and groundwater on the slope failures triggered by earthquakes.

1.2 Objective and scope

This research aims to investigate the failure mechanism and the influence of the soil behavior and groundwater on the shallow landslides triggered by the 2018 Hokkaido Eastern Iburi Earthquake and 2018 Western Shimane Earthquake.

The major objectives of the research projective are as follows:

(1) To classify the types and geometry features of the Iburi landslides by field investigation;

(2) To analyze the correlation between Iburi landslide distribution and thickness of Ta-d pumice with the aid of ArcGIS;

(3) To investigate the soil composition of the Iburi landslides and Kataragai landslide through vertical stratigraphic sections, in-situ hardness test, and portable penetration test;

(4) To study the physical properties, shear behavior and anti-liquefaction strength of the sliding mass through conventional physical test, consolidated-undrained triaxial compression test, and consolidated-undrained cyclic loading triaxial test;

(5) To determine the groundwater table in the crown of Kataragai landslide and confirm the existence of the seepage through the self-potential test;

(6) To analyze the failure mechanism of the Iburi landslides and Kataragai landslide;

(7) To explore the factors controlling the occurrence and distribution of the Iburi landslides and Kataragai landslide.

1.3 Thesis structure

This thesis focuses on the controlling role of the soil and groundwater on landslide triggered by the 2018 Hokkaido Eastern Iburi Earthquake and 2018 Western Shimane Earthquake.

Chapter 1 reviews previous research on the earthquake-triggered landslides and the research purpose of this work.

Chapter 2 describes the 2018 Hokkaido Eastern Iburi Earthquake and 2018 Western Shimane Earthquake and the geological conditions as well as preceding rainfall conditions in the affected region.

Chapter 3 explains the rationale for the methodology adopted in field investigation and laboratory tests.

Chapter 4 presents the types and features of Iburi landslides and the results of in-situ tests and laboratory tests of the Iburi landslides.

Chapter 5 presents the features and results of in-situ tests and laboratory tests of Kataragai landslides.

Chapter 6 discusses the controlling role of the soil and groundwater on landslide triggered by the 2018 Hokkaido Eastern Iburi Earthquake and 2018 Western Shimane Earthquake.

Chapter 7 concludes the thesis by highlighting several conclusions of the Iburi landslides and Kataragai landslides.

Earthquakes and geological setting

2.1 Hokkaido Eastern Iburi earthquake

2.1.1 Introduction of Hokkaido Eastern Iburi earthquake

At 03:07:59.3 (JST) on September 6, 2018, a Mj 6.7 (Mw 6.6) earthquake (Japan Meteorological Agency (JMA) scale) struck the Eastern Iburi region of Hokkaido, Northern Japan. The epicenter of the mainshock is located at N 42°41.4′, E 142°00.4′, and the focal depth is approximately 37 km (Japan Meteorological Agency (JMA) 2018a). A maximum seismic intensity of 7 on the JMA scale and a peak ground acceleration (PGA) of 1.84 g (HKD127 K-NET station in Fig. 2.1b) were reported. After the mainshock, a sequence of persistent aftershocks occurred. Three hundred and eleven aftershocks with a maximum seismic intensity larger than 1.0 were reported by JMA up to the 31st of October 2018. The focal mechanism of the mainshock of the Iburi earthquake has been investigated based on the InSAR interpretation and the focal mechanism solution. Kobayashi et al. (2019) concluded that the Iburi earthquake was induced by the displacement of a steep reverse fault on a plane dipping eastward at 74° after analyzing the ALOS-2 SAR data before and after the earthquake. The aftershock distribution and the focal mechanism solution indicate that the seismogenic rupture initiated as a small left-lateral strike-slip fault in the stepover segment, and two large reverse faulting ruptures occurred thereafter (Katsumata et al. 2019). Both seismogenic models are characterized by an N–S trending strike and deep focal depth.
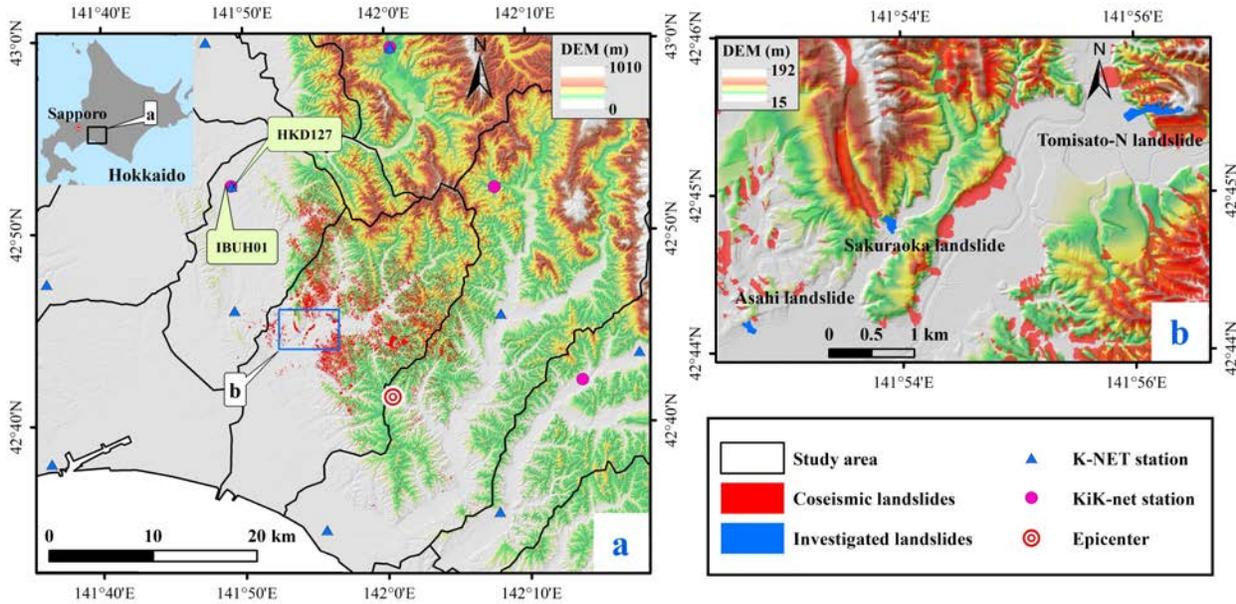
Fig. 2.1 Location maps. **a** Coseismic landslide triggered by 2018 Hokkaido Eastern Iburi Earthquake; **b** Distribution of three investigated landslides. The Iburi landslide database is derived from Zhang et al. (2019a)

During the Iburi earthquake, 41 people were killed and 691 people were injured; 394 houses were completely destroyed and 1,061 houses were damaged (based on reports by the Ministry of Internal affairs and Communications, Japan). The catastrophic Iburi earthquake caused extensive liquefaction in Sapporo and widespread damage to dwelling houses as well as the infrastructures. The electric power facilities in the afflicted region were greatly damaged by the strong seismic shaking. Multiple consecutive factors such as the shutdown of the Tomato-Atsuma electric power plant, and the shutdown of the hydroelectric power plants due to trouble in electric power lines, led to the long-term blackout in the whole Hokkaido area of 2,950,000 houses at 03:25 on September 6, 2018, 18 minutes after the mainshock (Cabinet office 2018; Organization for Cross-regional Coordination of Transmission Operation, Japan 2018; Takahashi and Kimura 2019). However, the most attractive and striking event was the massive occurrence of the coseismic landslide and its immense damage to the local residents. More than 5,000 landslides were simultaneously triggered by the strong ground motion, and the total affected area was 46.3km^2 (Zhang et al. 2019a). The high-mobilized and long run-out landslides are responsible for

approximately 88% of the causalities (36 out of the 41 deaths) in the Iburi earthquake (Yamagishi and Yamazaki 2018; Osanai et al. 2019).

2.1.2 Geological setting

Due to the subduction of the Pacific and Philippine plates to the Eurasian plate, Japan is recognized as a country inflicted by frequent earthquakes. The southwest Hokkaido, where the Iburi earthquake is located, is subjected to the northwestward subduction of the Pacific Plate and convergence between the North American and the Eurasian Plates (Kimura 1994; Tamaki et al. 2010). Faults with NNW-SSE and NW-SE strikes are extremely developed in this region. Considerable historical earthquakes have occurred in this region, although the seismic frequency is much lower than those on the eastern coast and the Kuril trench. Figure 2.2 illustrates the historical earthquakes that occurred 50 years prior to the Iburi earthquake in the landsliding area and its vicinity, and only earthquakes with a magnitude larger than 5.0 are depicted. The 2017 M_w 5.3 earthquake occurred in the Iburi landslide distribution area, and another five earthquakes (the 2009 M_w5.5 earthquake, the 2007 M_w5.5 earthquake, the 1981 M_w6.3, and M_w5.0 earthquakes, and the 1978 M_w5.0 earthquake) occurred less than 20km from the landslide affected area.
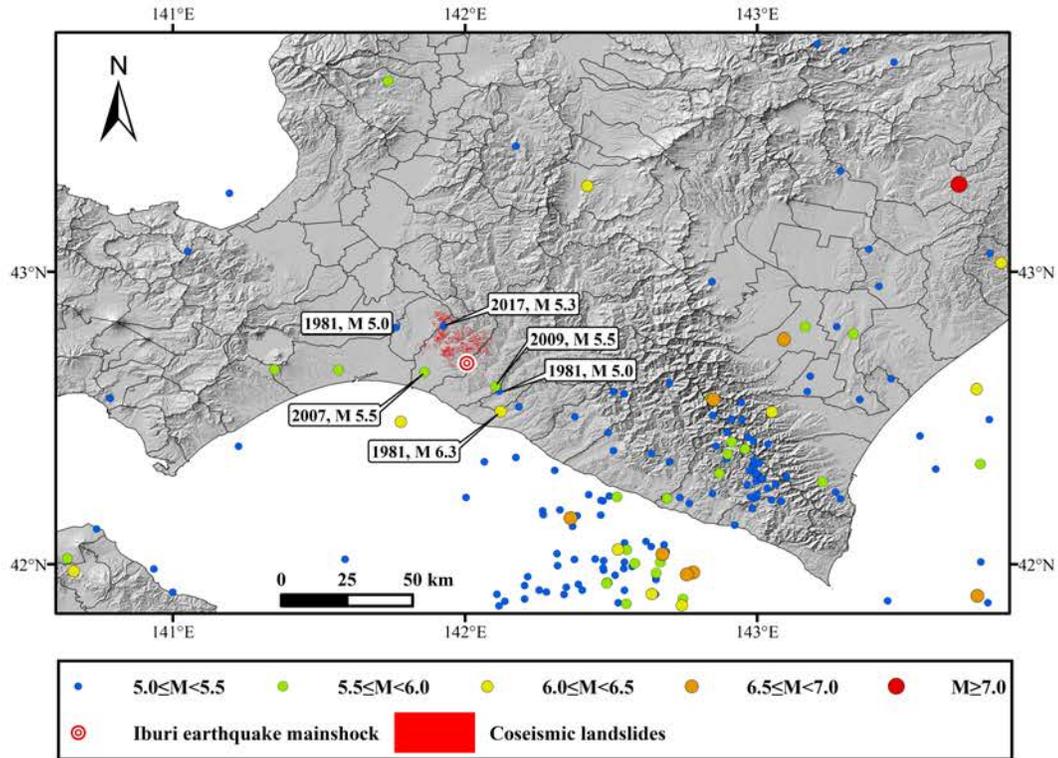
Fig. 2.2 Historical earthquakes (M≥5.0) occurred 50 years prior to the Iburi earthquake around the study area. The seismic data are derived from the United States Geological Survey (USGS)

The Iburi landslides mainly occurred in the hilly terrain at an elevation lower than 350 m and a slope angle less than 30°. Human activities and residence chiefly concentrate on the fluvial plains. The outcropped strata in the Iburi landslide-affected area are shown in figure 2.3. The outcropped strata are dominated by Neogene and Quaternary marine and non-marine sedimentary rocks and Late Pleistocene non-alkaline pyroclastic flow volcanic rocks (Ozaki and Taku 2014). The Iburi landslides are primarily distributed in the area with the bedrock of Middle Miocene to Pliocene mudstone, siltstone, sandstone, and conglomerate (Zhang et al. 2019a).
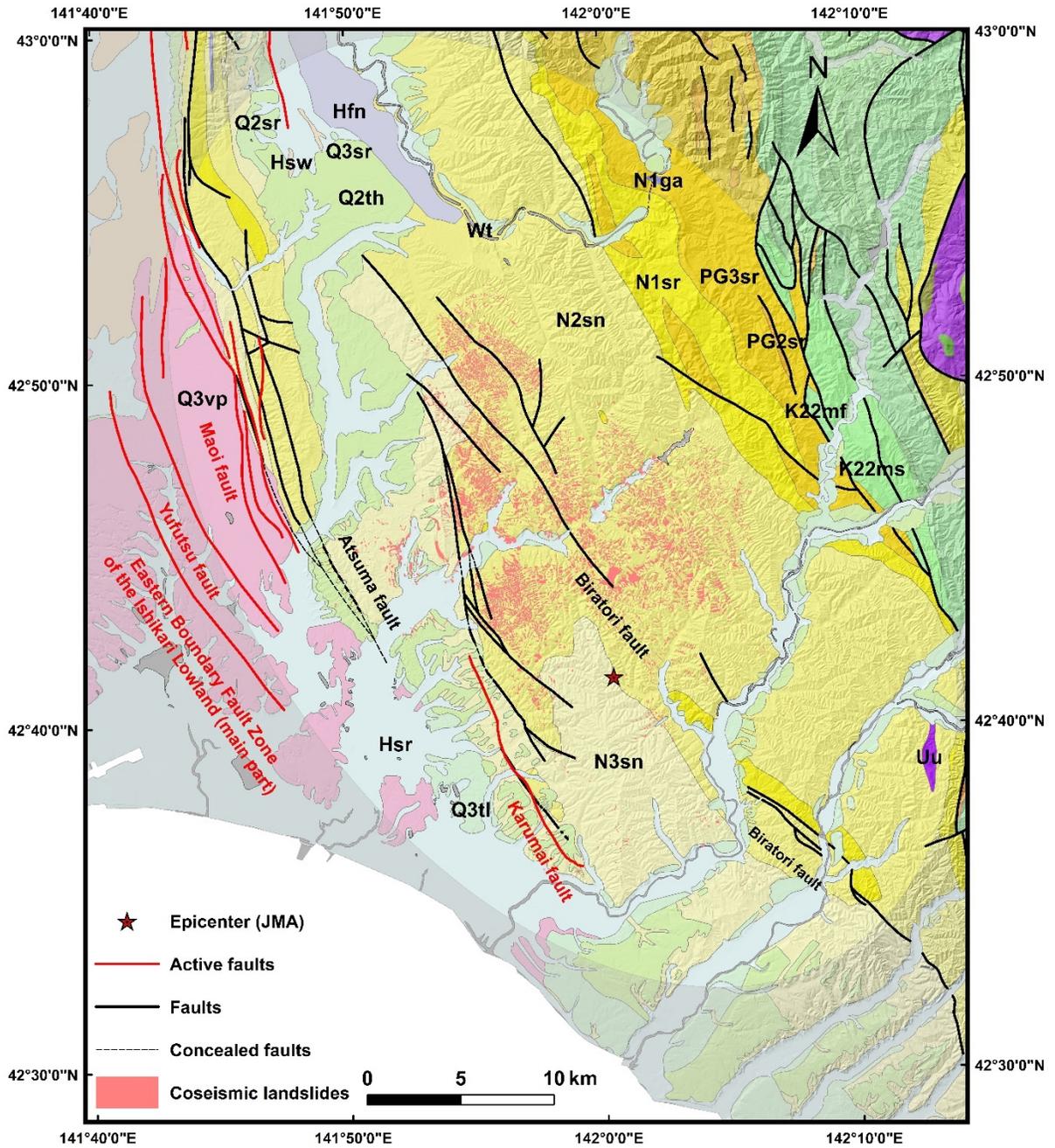
Fig. 2.3 Geological setting of the study area. Geological units and (active) faults are categorized based on the 1:200,000 seamless geological map published by the Geological Survey of Japan, AIST. (Zhang et al. 2019)

The pyroclastic fall deposits (volcanic ash, pumice, and scoria) covering the study area mainly originate from Tarumae, Eniwa, Shikotsu, and Kuttara calderas (Yamagata 1994; Osanai et al. 2019). The uppermost deposits in the landslide area are the pyroclastic fall deposits from the Tarumae volcano. The vertical stratigraphic section in Fig. 2.4 is a representative section revealing the composition of the pyroclastic fall deposits in the study area. Since the study area is distant from the Tarumae volcano, pyroclastic flow deposits can rarely be observed. Based on the eruptive history of the Tarumae, the pyroclastic fall deposits of Tarumae are divided into four layers: the Tarumae a (Ta-a: 1739 A.D.), Tarumae b (Ta-b: 1667 A.D.), Tarumae c (Ta-c: 2.5 ka), and Tarumae d (Ta-d: 8.7–10 ka) (Furukawa and Nakagawa 2010; Tajika et al. 2016). The Ta-a consists of a mixture of scoria and gray pumice (Tajika et al. 2016). Ta-b is comprised of gray pumice with a clear bedding structure, and the particle size decreases top-down. The humus layer between the Ta-a and Ta-b can rarely be observed due to the short eruption interval. The Ta-c originates from three eruptions around 2.5 ka ago (Furukawa and Nakagawa 2010), and the Ta-c2 from the second eruption layer is widely spread in the landslide area. Ta-c2 is mainly composed of fine-grained gray volcanic ash (Furukawa and Nakagawa 2010). Humus layers are occasionally sandwiched in the interfaces between Ta-c and Ta-b as well as Ta-c and Ta-d (Osanai et al. 2019). The Us-b pyroclastic deposits from the nearby Usu volcano and the B-Tm fine-grained pumice from the Baekdu mountain can sometimes be observed between Ta-b and Ta-c in the vicinity of the landslide area. Ta-d is the most widely distributed layer in the study area, and it is determined to be approximately 8.7 to 10 ka old based on the carbonized plants buried at the bottom of the Ta-d layer (Furukawa and Nakagawa 2010). Ta-d is composed of two layers, i.e., the upper dark gray coarse scoria (Ta-d1) and the lower porous pumice (Ta-d2). The soil layer underlying the Ta-d layer is the hard and dense silty paleosol with poor permeability. The sliding mass of the Iburi landslide is mainly comprised of the pyroclastic fall deposits mantled on the hard paleosol. Besides, some pyroclastic fall deposits, i.e., Eniwa-a (En-a: 19–21 ka), Shikotsu (Spfa-1 and Spfa-2: 40 ka) and Kuttara (Kt-1: 43.5 ka), originated from the Eniwa and the Shikotsu caldera (Furukawa and Nakagawa 2010), are located between the Ta pumice and the bedrock.
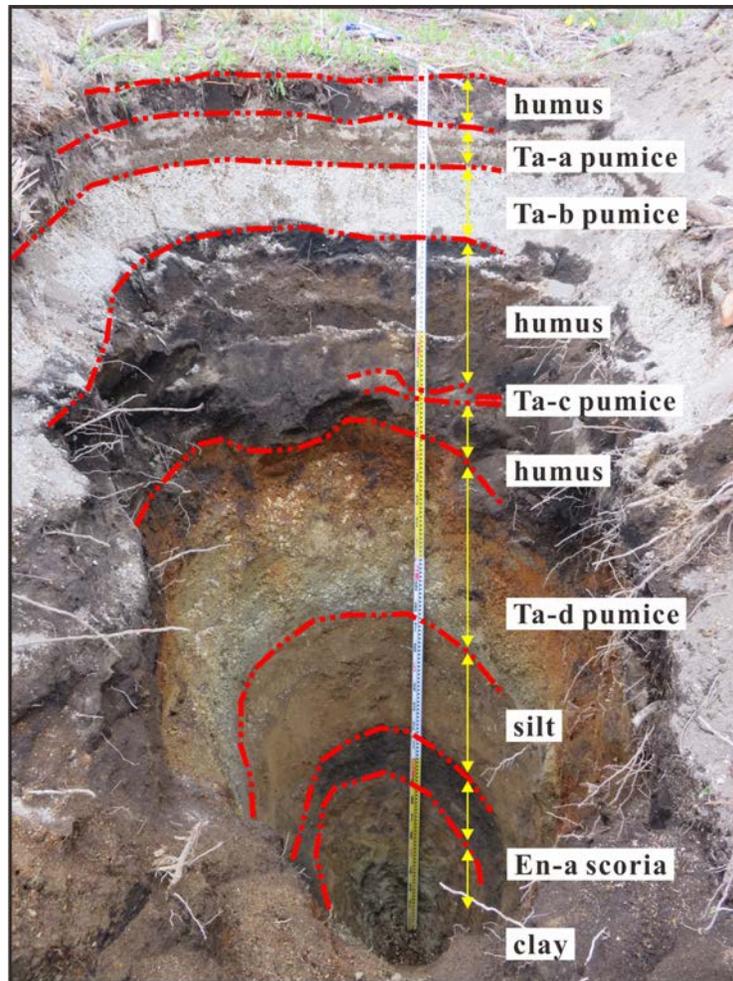
Fig. 2.4 A typical vertical stratigraphic section presenting the composition and structure of the pyroclastic fall deposits in the study area

Based on the field investigation, most of the 5,625 Iburi landslides, except for the two deep-seated landslides, are characterized by the overall sliding of the surficial and shallow pyroclastic fall deposits, and the sliding zone is located in the Ta-d2 pumice over the hard paleosol. To study the correlation between the Iburi landslide occurrence and pyroclastic fall deposits, the isopachs of the pyroclastic fall deposits originating from the Tarumae mountain are depicted in Fig. 2.5. The isopachs of the Ta-d2 pumice are closely related to the spatial distribution of the Iburi landslides. It should be noted that the isopachs of the pyroclastic fall deposits in Fig. 2.5 do not strictly and exactly match the thickness and the distribution of the

pyroclastic fall deposits in the study area. It was observed in the field survey that the thickness and completeness of the pyroclastic fall deposits vary even in one landslide. Even so, these isopachs can provide a reasonable reference for the analysis of the correlation between pyroclastic fall deposits and the Iburi landslide.
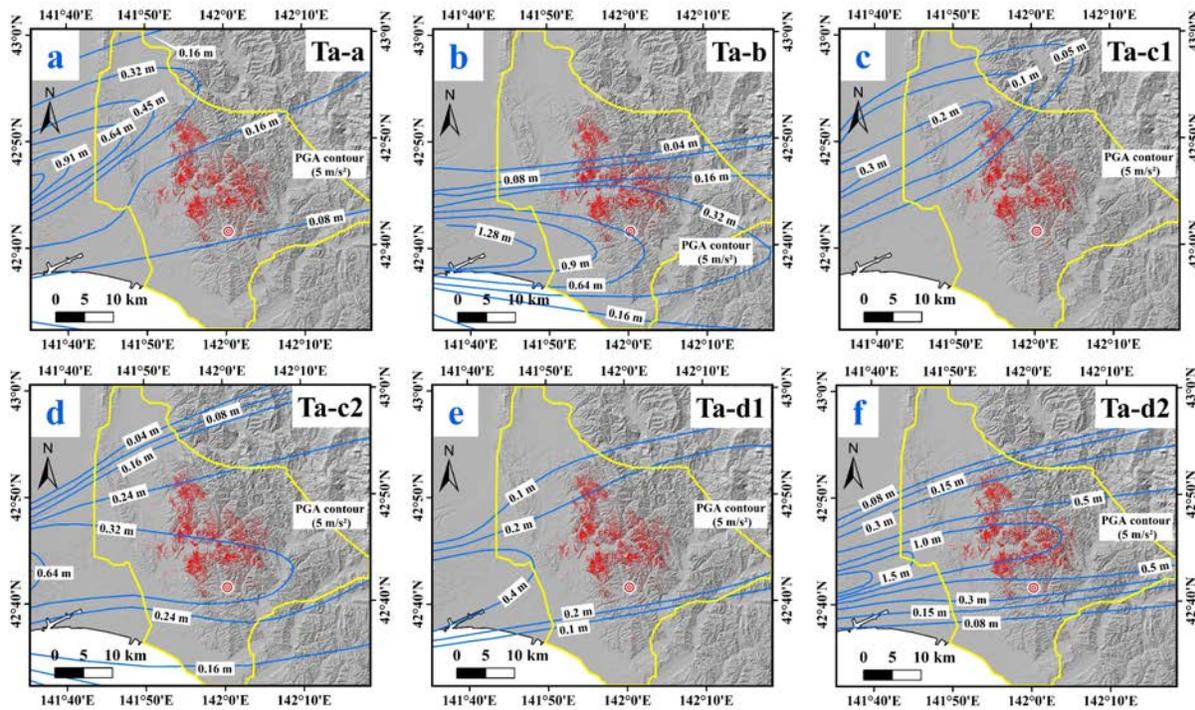
Fig. 2.5 Isopach maps of the pyroclastic fall deposits originated from Mounts Tarumae. The isopachs are based on Furukawa and Nakagawa (2010)

To study the effect of Ta-d pumice on the Iburi landslide occurrence, the irregular polygon with PGA larger than 5 m/s^2 (Fig. 2.5) was selected as the targeted area, as the PGA is widely considered as the predominant factor controlling the occurrence of the coseismic landslides (Liao and Lee 2000; Gorum et al. 2013; Xu et al. 2015). A 5-m/s^2 PGA contour was generated based on the PGA map provided by the Quick Estimation System for Earthquake Map Triggered by Observed Records (https://gbank.gsj.jp/QuiQuake/QuakeMap/20180906.en.html). Approximately 98.9% (5561) of the coseismic landslides (5625) are encompassed by the 5-m/s^2

PGA contour. To study the relationship between the thickness of the Ta-d2 layer and the occurrence of the Iburi landslides, the targeted area is divided into six subareas based on the isopachs of the Ta-d2 thickness. In this work, two terms—landslide area density (*LSAD*) and landslide number density (*LSND*)—are used to describe the density of landslides occurring in each subarea, and the corresponding equations are expressed in Eqs. 2.1, 2.2. Obviously, both the *LSAD* and *LSND* increase with an increase in the thickness of the Ta-d2 pumice despite the subarea with a thickness of less than 0.08 m being the largest class (Fig. 2.6). The positive correlation between landslide density and Ta-d2 thickness demonstrates the important role of Ta-d pumice on the occurrence and distribution of the Iburi landslides.

$$LSAD = \frac{LSAP}{CAP} \times 100\% \qquad (2.1)$$

$$LSND = \frac{LSNP}{CAP} \times 100\% \qquad (2.2)$$

Where *CAP* is the percentage of a certain class (subarea) area to the targeted area, *LSAP* is the percentage of the landslide area in a certain subarea to the total landslide area, and *LSNP* is the percentage of the landslide number in a certain subarea to the total landslide area.
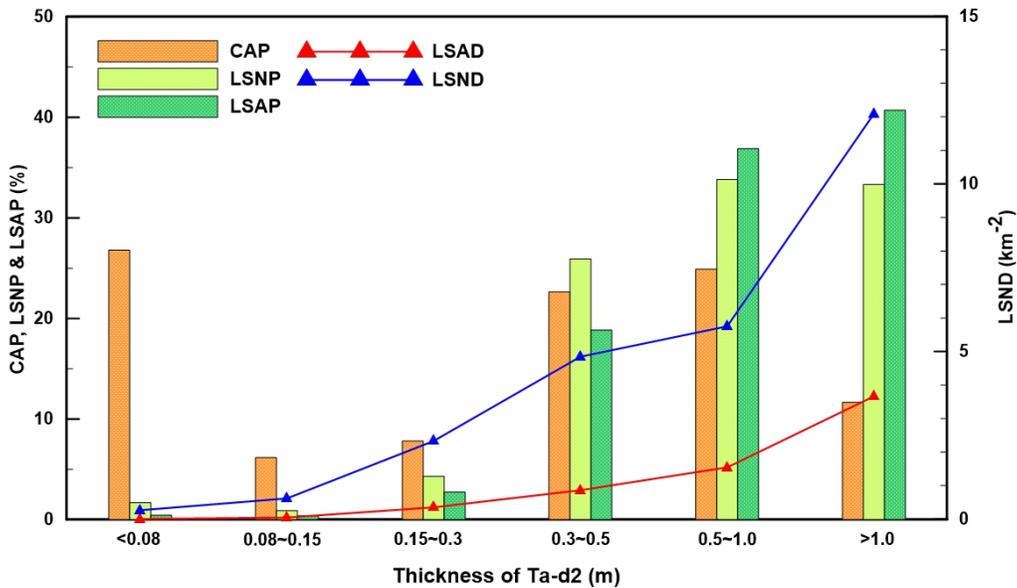
Fig. 2.6 Relationships between the thickness of Ta-d2 and the occurrence of the Iburi landslides in the corresponding class

2.1.3 Preceding rainfall

It is widely accepted that the precipitation accompanying strong ground motion will enhance the possibility and severity of coseismic landslides, and the liquefaction during an earthquake will be intensified. Figure 2.7 displays the monthly precipitation in 2018 and the 30-year mean precipitation between 1989 and 2018 in the vicinity of the study area. The localities of the four AMeDAS stations are shown in Fig. 2.1b. Clearly, the monthly precipitations in July, August, and September are much higher than in other months. The Iburi earthquake on September 6 occurred in the rainy season, and the monthly precipitations in July and August 2018 are much higher than the mean precipitations of the past 30 years. The precipitation in August 2018 is more than 200 mm, which provides the hydrological condition for the wide occurrence of the Iburi landslides. The groundwater table was elevated especially in combination with the persistent and torrential rainfall in July and August. The elevated groundwater table further increases the liquefaction potential and the possibility of wide-spread coseismic landslides.
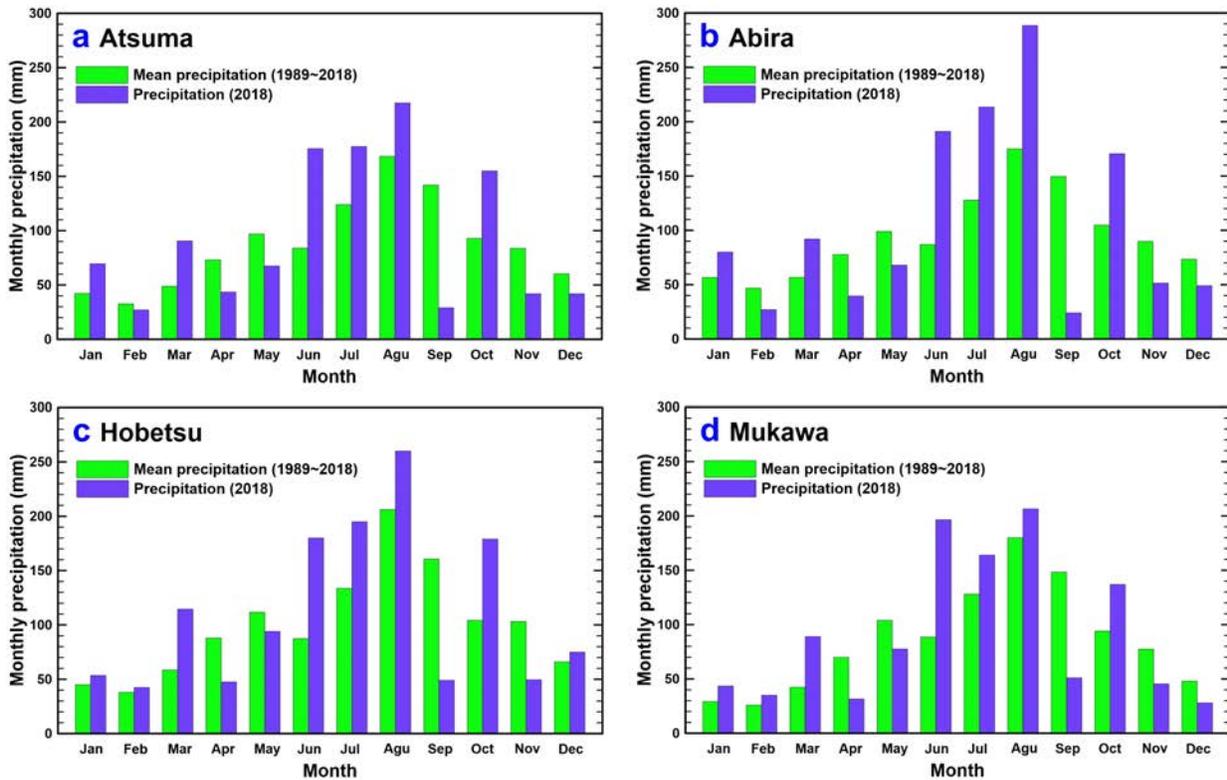
Fig. 2.7 Monthly precipitation in 2018 and 30-year mean precipitation (1989 to 2018) of four AMeDAS stations in the vicinity of the study area. The location of the AMeDAS stations are illustrated in Fig. 2.1b

2.2 Western Shimane earthquake

2.2.1 Introduction of Western Shimane earthquake

A M 6.1 (M_w 5.7) earthquake with a focal depth of approximately 12 km struck Oda, Shimane, Japan, at 1:32 (JST) on April 9, 2018 (Japan Meteorological Agency 2018b; Geospatial Information Authority of Japan, GSI, 2018). The epicenter of the 2018 Western Shimane Earthquake is located at 35.2° N, 132.6° E and the maximum seismic intensity is 5.0 according to the Japan Meteorological Agency (JMA) seismic intensity scale (Japan Meteorological Agency 2018c). A peak ground acceleration (PGA) of 6.762 m/s^2 was observed in a K-NET station (SMN006) approximately 8.0 km from the epicenter (National Research Institute for Earth Science and Disaster Resilience (NIED) 2019). Figure 2.8 depicts the area suffered from intense ground motion during the earthquake.
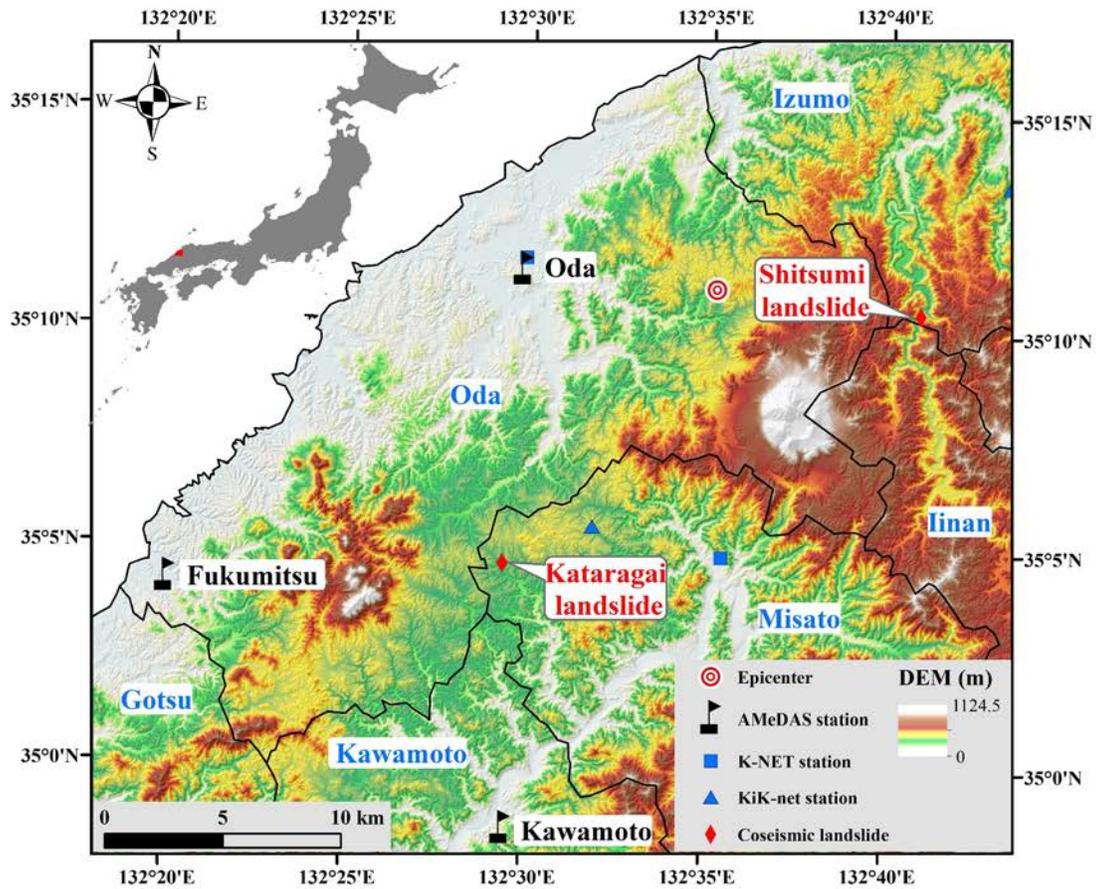
Fig. 2.8 Location map and coseismic landslides triggered by the 2018 Western-Shimane earthquake

During the Western-Shimane earthquake, 7 people (2 serious wounds and 5 slight wounds) were injured and 38 houses were completely ruined during the strong ground motion according to the Fire and Disaster Management Agency, Japan. Two landslides (the Kataragai landslide and the Shitsumi landslide) were triggered in the 2018 Western Shimane Earthquake (Fig. 2.8). The Kataragai landslide, approximately 17 km southeast to the epicenter, occurred in a gentle slope with a slope angle of approximately 7°, and the Shitsumi landslide with an epicentral distance of approximately 8 km occurred in a steep slope beside a highway. Figure 2.9 illustrates the distribution maps of the PGA and seismic intensity of the 2018 Western Shimane Earthquake in

the study area. Clearly, both Kataragai landslide and Shitsumi landslide are not distributed in the area suffered from the most intense ground motion. The occurrence of the Kataragai landslide and the Shitsumi landslide seems to be controlled more by the topographic, geological, and hydrological conditions.
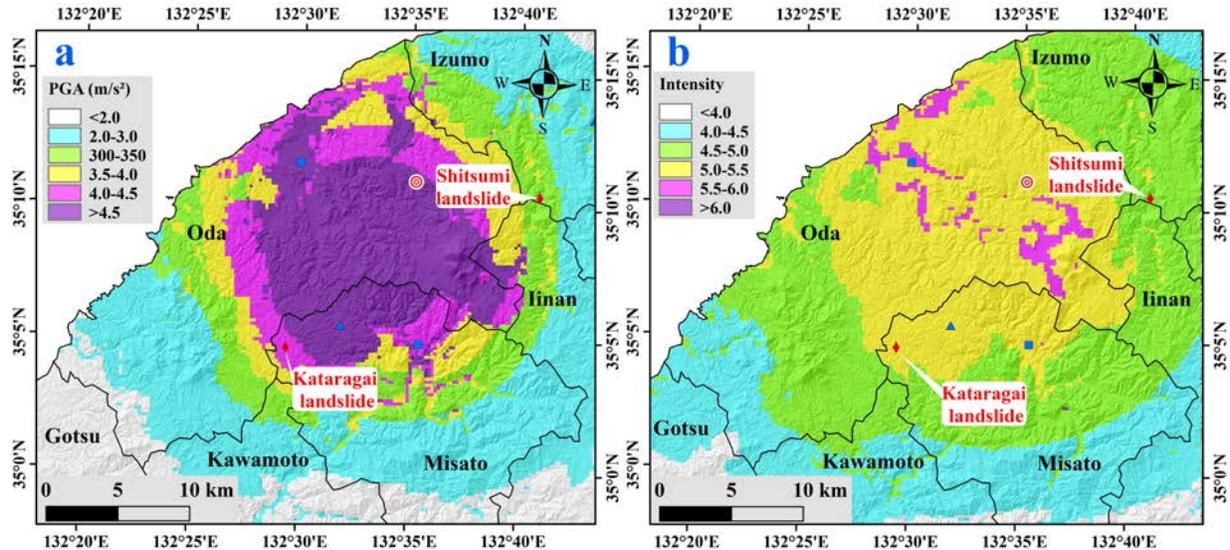
Fig. 2.9 Peak ground acceleration (PGA) (**a**) and seismic intensity (**b**) of the 2018 Western-Shimane earthquake

2.2.2 Geological setting

The epicenter of the 2018 Western-Shimane earthquake is located near to the east coast of the Japan Sea. The elevation of the study area ranges from 0 to 1124.5 m and the northwest part is characterized by a flat plain. The topography generally southeastward escalates to hilly terrain with slope angle mainly between 10° to 40°.

Based on the 1:200,000 geological map of Hamada (https://www.gsj.jp/data/200KGM/JPG/GSJ_MAP_G200_NI5332_1988_200dpi.jpg), the main strata of the study area can be generally classified into three types. The nethermost layer is

composed of the Early Miocene Andesite lava and pyroclastic rock (Hata Formation and its equivalent). The middle layer is represented by the Late Pliocene Gravel Bed gravel, sand, and mud constitute (Tsunozu Group and Kotachi Gravel Bed). The surface layer is the Early Pleistocene dacite pyroclastic deposits (Products of Oetakayama Volcano). The faults distributed in the study area are mostly developed with a NE-SW strike.

The Kataragai landslide is situated approximately 17 km southwest to the epicenter, and the main scarp of the Kataragai landslide is at 35.078° N, 132.491° E. As is illustrated in Fig. 2.9, the Kataragai landslide lies in the area with a PGA between 4 m/s^2 and 4.5 m/s^2, and the seismic intensity of the Kataragai landslide is approximately 5.0. The elevation of the slope where the Kataragai landslide is situated ranges from 200 m to 240 m and the slope angle is approximately 7°. Outcropped bedrock can not be observed in the slope, and the bedrock is mantled with medium sand with gravel. The Kataragai landslide occurred in an artificial slope refilled after the clay mining according to the local residents. For the benefit of conservation of water and soil, several ponds were constructed in the slope, and the surface water and the groundwater could be impounded. Perennial water could be observed in ponds during the fieldwork.

2.2.3 Preceding rainfall

Based on rainfall data delivered by Japan Meteorological Agency, daily and cumulative precipitation of three available AMeDAS stations (Fig. 2.8) during the period of 9 March 2018 to 14 April 2018 are depicted in Fig. 2.10. The Western-Shimane earthquake was accompanied by a small amount of rainfall in the study area. Figure 2.10 illustrates that the study area experienced prolonged rainfall during the period from 19 March to 21 March. The cumulative rainfall recorded by the three stations in one month before the earthquake is between 140 mm and 180 mm. Persistent rainfall in August may greatly contribute to the occurrence of landslides during the intense ground shaking of the Iburi earthquake. The precipitation contributes to the rise of the groundwater table and further increases the liquefaction potential and the possibility of a landslide.
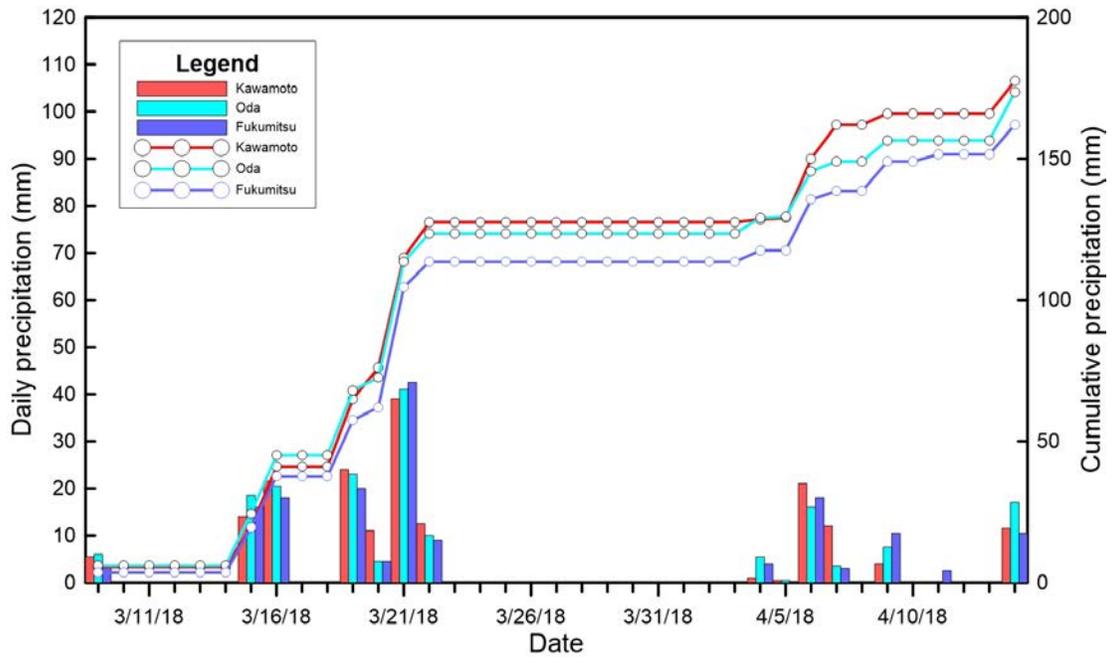
Fig. 2.10 Daily and cumulative precipitation from 9 March 2018 to 14 April 2018

Methodology

3.1 Field survey

To investigate the soil composition and the failure mechanism of the Iburi landslides, three concentrated field surveys were conducted in September 2018 and May and June 2019. The investigations cover not only on-site fieldwork, but also the visit to a local geological museum and the inquiries of local residents. During the field reconnaissance of Iburi landslides, profile measurements, vertical stratigraphic section investigation, and hardness tests were performed. Based on the longitudinal and vertical stratigraphic sections, the types of the Iburi landslides are classified. Three different types of shallow debris landslides were studied in detail. Based on the field investigation, the characteristics and types of shallow debris slides, the soil composition and variation of sliding mass in the vertical direction, the location of the sliding zone, and the initiation and motion features of different types of landslide are elaborated.

The fieldwork on the Kataragai landslide was conducted in detail two days after the 2018 Western-Shimane earthquake. During the field reconnaissance, profile measurements, portable penetration tests, vertical stratigraphic section investigation, and hardness tests were performed to study the soil composition and variation in the vertical direction, and locate the sliding zone. The landslide boundary was confirmed through the aerial image and the GPS points localized in the field. Meanwhile, the self-potential test was carried out to confirm the existence of the seepage at the crown.

3.1.1 Hardness test

The hardness tests could be used to preliminarily evaluate the variation of the uniaxial compressive strength with depth for the soil layer. In this work, the hardness tests were conducted in a vertical section. Hardness test was conducted five times for each soil layer, and the average of the three results without the maximum and minimum were finalized as the test results.

3.1.2 Portable dynamic cone penetration test

The portable dynamic cone penetration tests are performed to classify the soil with different strength (Yang et al. 2015a) and detect the potential sliding zone. During the portable dynamic cone penetration tests, a 5-kg hammer was dropped (free fall) from a height of 0.5 m. The number of drops (N_d) was recorded for a penetration depth of each 0.1 m (Qureshi et al. 2009). The number of drops (N_d) in the portable dynamic cone penetration test can be converted to the number of drops (N) in the standard penetration test using Equation 3.1.

$$N = N_d/1.5 \tag{3.1}$$

In addition to determine the boundaries of soil layers, the penetration test results can be utilized to evaluate the anti-liquefaction strength preliminarily. The anti-liquefaction evaluation is applicable for a depth within 20 m. The critical value of standard penetration blow count for liquefaction evaluation (N_{cr}) can be calculated using Equation 3.2 (CMC 2010; Liu 2016).

$$N_{cr} = N_0\beta[\ln(0.6d_s + 1.5) - 0.1d_w]\sqrt{3/\rho_c} \tag{3.2}$$

where N_0 is the reference value adopted according to different design basic accelerations, which may be adopted according to Table 3.1; d_s is the depth of standard penetration point for saturated soil (m); d_w is the groundwater level (m); ρ_c is the percentage content of sticky particles, which shall be taken as 3 if less than 3 or the soil is sandy soil; β is the adjustment coefficient, which

shall be taken as 0.80 for design earthquake group 1, 0.95 for group 2, and 1.05 for group 3. The design earthquake group is related to the characteristic period of acceleration response spectrum. When the characteristic periods are 0.35 s, 0.40 s and 0.45 s, the design earthquake groups are design earthquake group 1, design earthquake group 2 and design earthquake group 3, respectively.

Table 3.1 Reference value (N_0) of standard penetration blow count for liquefaction evaluation

Design basic acceleration of ground motion (g)	0.10	0.15	0.20	0.30	0.40
N_0	7	10	12	16	19

By substituting Equation 3.1 into Equation 3.2, the critical value of portable dynamic cone penetration test blow count for liquefaction evaluation (N'_{cr}) can be calculated using Equation 3.3.

$$N'_{cr} = 1.5N_0\beta[\ln(0.6d_s + 1.5) - 0.1d_w]\sqrt{3/\rho_c} \tag{3.3}$$

3.1.3 The self-potential test

The self-potential (SP) method is a passive geophysical technique that responds to naturally occurring potentials on the earth surface. In a saturated system, the potential difference is 0 under static conditions as the electric charges across the solid-fluid interface maintain an equilibrium.

When liquid flows, a charge imbalance appears due to the exchange of the charged ions across the solid-fluid interface, and the potential difference is generated (Ishido et al. 1983). Generally, the flow carries the electropositive ion downstream. Thus, a negative SP is generated on the flow path and a positive SP appears in the downstream area. The SP method has been adopted for monitoring seepage, internal erosion, and piping in landslide dams and levees (Corwin 1991; Moore et al. 2011; Thompson et al. 2012; Wang et al. 2018). In this work, two sets of self-potential tests were performed along survey lines C-C′ and D-D′ (Fig. 3) using the fixed-base method (Lowrie 2007). Point C and point D were selected as the base points and the potential difference between the base point and other points in the same survey line was measured accordingly. The potential difference between points C and D was also measured. For easy comparison, the potential difference between each point and point C is regarded as the potential of the corresponding point. Then, the location of the seepage flow in the slope could be determined.

3.2 Laboratory investigation

The geotechnical properties of the soil (sliding mass) primarily control the failure mechanism of the landslide. To obtain the basic physical properties (in-situ density, dry density, water content, specific gravity, void ratio, and degree of saturation) of the soils, relevant laboratory tests were conducted. In this work, samples in different layers taken from the landslide crown were regarded as the main objectives. The basic physical properties of all samples were obtained, and only samples around the sliding zone were employed in the grain size analysis and the triaxial tests. All the tests in this work were carried out based on the standards of the Japanese Geotechnical Society (JGS 2010).

3.2.1 Static consolidated-undrained triaxial compression test

The consolidated-undrained triaxial compression test is a common method to investigate the soil behavior and the stress-strain behavior of the soil can be obtained in this test (Wang et al. 2015; Yang et al. 2015a; Xu et al. 2018b). The consolidated-undrained triaxial compression test is

generally divided into two steps, i.e., specimen preparation and test implementation. In the specimen preparation stage, by controlling the dry density identical to corresponding undisturbed soils, remolded specimens were constructed in a cylindrical rubber membrane with a height of 100 mm and a diameter of 50 mm. When constructing the remolded specimens, only soils passing through the 4.75-mm sieve were used as the grain size of the specimen should be less than 10% of the specimen diameter (50 mm). After exhausting the air in the specimen with carbon dioxide completely, the de-aired water was gradually supplied to fully saturate the specimen. Generally, the Skempton's B value (Skempton 1954; Ortigao et al. 1995) is used to evaluate the degree of saturation in the triaxial test, and the specimens can be considered to be fully saturated when the Skempton's B value is larger than 0.95 (Sassa 1985; Tokimatsu et al. 1990; Yang et al. 2015b). After the specimens being fully saturated, the specimens were consolidated under the confining stress (σ_0) of 30 kPa, 40 kPa, or 50 kPa.

In the test implementation stage, the specimens were compressed under the undrained condition with an axial strain of 1.0% per minute and the axial stress increment ($\Delta\sigma=\sigma_1-\sigma_0$) as well as the pore water pressure (u) could be obtained. The shear strengths of specimens under different confining stress were obtained through the effective stress path and the critical state line (CSL).

3.2.2 Cyclic consolidated-undrained triaxial compression tests

As confirmed in several previous cases, the shallow flow slide that occurred in the earthquake is always related to the cyclic liquefaction in soil (Seed 1968; Ishihara et al. 1990; Harp et al. 2003; Pei et al. 2017). In this work, the unidirectional cyclic triaxial (CTX) apparatus was employed in the CTX strain-controlled testing and the anti-liquefaction strength of the specimen from the Kataragai landslide was investigated. The same specimen preparation procedure applied in the static triaxial test was utilized in the CTX tests. After the consolidation with confining stress of 40 kPa, a sinusoidal cyclic axial load was applied at a frequency of 1.5 Hz to the specimen under the undrained condition and the stress variation on a plane dipping at 45° was used to simulate the cyclic shear stress applied to the soil during the intense ground motion. In the CTX test, the confining stress should be corrected to keep the normal stress on the 45°-dipping plane a constant value. Since only pore pressure was affected by the variation of the confining stress, the

corrected pore pressure ratio (r_u) was used to describe the variation in the pore water pressure (Zlender and Lenart 2005; Xie 2011; Faris and Wang 2014). The corrected pore pressure ratio is defined in Eq. 3.4.

$$r_u = \frac{\Delta u - \frac{\Delta \sigma_1}{2}}{\sigma_0'} \tag{3.4}$$

where Δu is the increment of pore water pressure, $\Delta \sigma_1$ is the increment of axial stress, and σ_0' is the effective isotropic consolidation stress.

The anti-liquefaction strength of the soil is judged by the relationship between the cyclic shear stress (τ_d) and the number of cycles required for liquefaction (N_L). During the CTX test, the dynamic stress (σ_d) was applied to the specimen. The N_L when liquefaction occurs ($r_u = 1$) can be obtained by the variation curves of the pore water pressure ratio. Under identical consolidation conditions, multiple sets of N_L with different dynamic stress (σ_d) can be obtained by changing the dynamic stress (σ_d). The cyclic shear stress (τ_d) is calculated using Eq. 3.5. Then, the correlation between the cyclic shear stress ratio ($\frac{\tau_d}{\sigma_0'}$) and the logarithm of N_L ($\lg N_L$) can be obtained (Seed et al. 1975). If the number of cycles is same in the test, the magnitude of the cyclic shear stress ratio when liquefaction occurs reflects the anti-liquefaction strength of the soil.

$$\tau_d = \frac{1}{2} \sigma_d \tag{3.5}$$

where τ_d is the cyclic shear stress and σ_d is the dynamic stress.

Field survey and test results of Iburi landslides

4.1 Types and features of the Iburi landslides

Due to the differences in geomorphology, soil composition and thickness, vegetation, and other affecting factors, the Iburi landslides show diverse geometric features and forms. The landslides can be categorized into two major types (i.e., the shallow debris slide and the deep-seated landslide) based on the sliding surface location. Only two deep-seated landslides were confirmed, and the rest of the Iburi landslides are mainly shallow debris slides. In this work, the shallow landslides were regarded as the main objectives, and their typical characteristics were combed out. The shallow debris slides triggered by the Iburi earthquake mainly presented three forms, i.e., steep debris slide, gentle debris slide, and mobilization of V-shaped convergent sliding masses. Details and representative landslides of these three types of shallow debris slides were described and studied.

4.1.1 Steep debris slide

The Sakuraoka landslide (Fig. 2.1c) is a typical steep debris slide, and it is composed of two sub-landslides (Fig. 4.1). The alternately bright and dark stripes on the exposed planar sliding surface (Fig. 4.1a) at the upper slope indicate the mobilization direction of the pyroclastic fall deposits. The mean slope angle of the exposed sliding surface along the longitudinal section A-A′ is approximately 22° (Fig. 4.1b), and the mean slope angle of the exposed sliding surface along the longitudinal section B-B′ gradually decreases from 44° to 10° (Fig. 4.1c). The apparent mobilized friction angles (Sassa et al. 1996; Sassa et al. 2005) for the two sub-landslides are 10.1° and 8.6°, respectively. The sharp bulges near the roads in Figs. 4.1b, c result from the excavation during the disaster relief operations. According to the field survey and the longitudinal sections,

the source area and the deposition area of the Sakuraoka landslide are approximately bordered by the road where the topography changes sharply. For a steep debris slide, the whole source area is almost exposed due to the displacement of the main body on the steep slope.
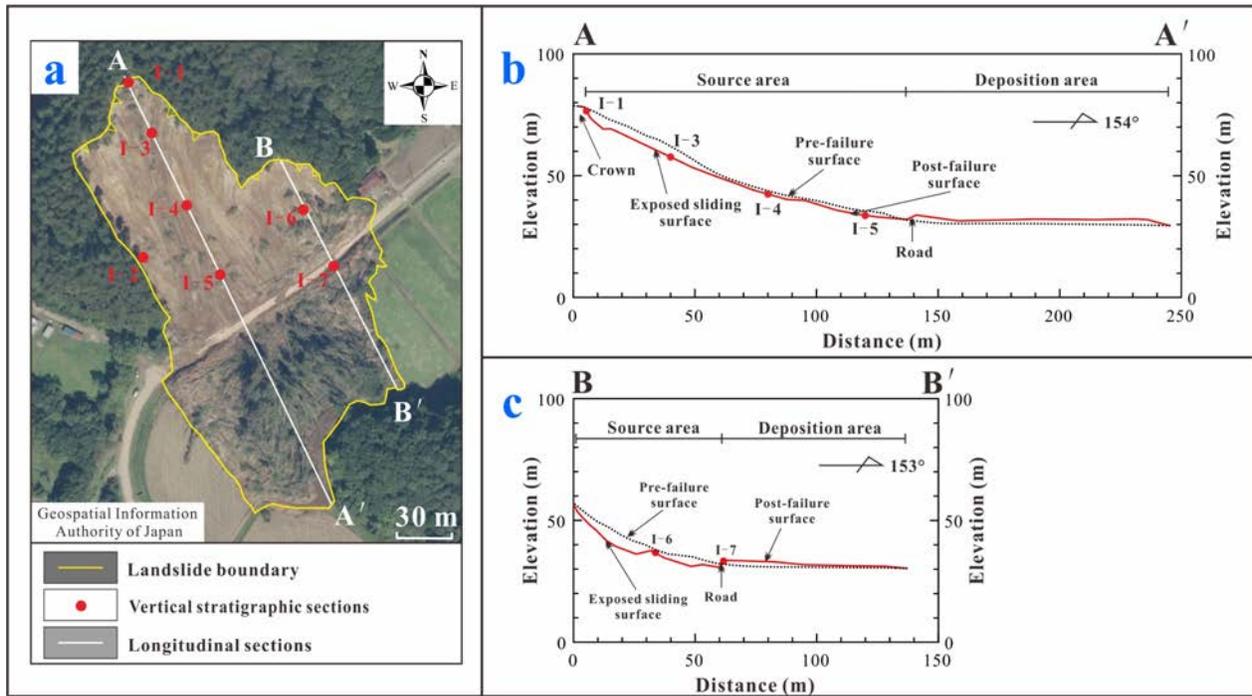
Fig. 4.1 The typical steep debris slide: Sakuraoka landslide. **a** General aerial view (the base map is derived from the Geospatial Information Authority of Japan). **b** Longitudinal section along survey line A-A′. **c** Longitudinal section along survey line B-B′

To investigate the soil structure and strength of the Sakuraoka landslide, a series of trenches were dug at the right boundary and along the survey lines (Fig. 4.1a), and two sets of in-situ hardness tests at the main scarp and the right boundary were conducted to obtain the uniaxial compressive strength. The hardness tests were conducted five times for each layer, and the average of the three tests without the maximum and minimum were calculated as the test results. The soil structure and the corresponding uniaxial compressive strength of the Sakuraoka landslide are shown in Fig. 4.2. At the main scarp of the Sakuraoka landslide (Fig. 4.2a), the Ta-a pumice and

the Ta-b upper coarse pumice were not observed, and the off-white Ta-b fine pumice layer was mantled with the 0.1-m-thick humus. The upper Ta-d layer (Ta-d1) was lost and the total thickness of Ta-d2 layer is approximately 2.45 m. The Ta-d2 pumice layer was further divided into five distinct sub-layers (Fig. 4.2a, b) based on the color, particle size, and particle strength. The top sub-layer is brownish-red, and the other four sub-layers are greyish-green. The brownish-red pumice layer (Ta-d pumice with volcanic ash) contains a certain amount of brownish-red volcanic ash and the volcanic ash content decreases top down. The grain size of the upper greyish-green pumice (Ta-d pumice MG) is coarse and decreases sharply at the bottom (Ta-d pumice FG and CS). While the Ta-d pumice FG and CS are the same soil layer in different locations (e.g., sections   -1 and   -2), their properties are different. The particle strength of the Ta-d pumice FG is high, but the Ta-d pumice CS is highly weathered and can be easily crushed with fingers. Several irregularly distributed soft and medium sandy pumice interlayers (Ta-d pumice MS) with different thicknesses can be found in Ta-d, and the water content of the cohesive medium sandy pumice is as high as 144% to 223%. As this Ta-d pumice MS interlayer can be observed in the stable main scrap and flank, it is inferred that the medium sandy pumice may result from the interbedded seepage flow parallel to the slope before the earthquake rather than the strong ground motion during the Iburi earthquake. The strength of the pumice layer was reduced due to the long-duration seepage flow, and the pumice layer was eroded and weathered to the powdered structure. The grain strength of the Ta-d pumice is relatively low compared to the Ta-a, Ta-b, and Ta-c layers. The nethermost layer in section   -1 is the silty paleosol, and one dark gray, coarse sand layer was observed in the silt layer. However, this coarse sand layer was not observed in other locations of the Sakuraoka landslide. The hardness test results in Fig. 4.2a show that the uniaxial compressive strength of the pyroclastic fall deposits varies with depth and reaches a minimum value in the Ta-d pumice MS. Then, the uniaxial compressive strength reaches a peak value in the bottom hard silt layer.

a I-1

NO.	Thickness (m)	Stratigraphy (si cs mg / ms fg)	soil name	color	particle size (mm)	others	Uniaxial compressive strength (kPa)
1	0.1		humus				
2	0.25		Ta-b pumice Ainu age	off-white	dominated by 1-4	porous grain, loose	
3	0.1		humus	black	fine	batt-like, loose	
4	0.15		Ta-c volcanic ash	off-white	1	loose	
5	0.7		Ta-d pumice with volcanic ash	brownish-red	dominated by 0.02-20	pumice with volcanic ash, porous grain, loose	
6	0.1		Ta-d pumice MS		0.3	medium sandy pumice, soft	
7	1.2		Ta-d pumice MG	greyish-green	dominated by 1-20	medium gravel, porous grain, loose	
8	0.3		Ta-d pumice MS		0.3	medium sandy pumice, soft	
9	0.15		Ta-d pumice FG		dominated by 1-5	fine gravel	
10	0.45		Paleosol (silt)	brownish-red	0.02	hard	
11	0.15		Paleosol (coarse sand)	dark gray	1	loose	
12	0.15		Paleosol (silt)	khaki	0.02	hard	

Depth (m): 0 – 3.8. UCS axis: 0, 200, 400

b I-2

NO.	Thickness (m)	Stratigraphy (si fg / cs mg)	soil name	color	particle size (mm)	others	Uniaxial compressive strength (kPa)
1	0.1		humus				
2	0.1		humus	black	fine	loose	
3	0.15		Ta-c volcanic ash	off-white	1	loose	
4	0.95		Jomon age humus	khaki	fine	loose, lower layer with gravel	
5	0.8		Ta-d pumice with volcanic ash	brownish-red	dominated by 0.02-20	pumice with volcanic ash, porous grain, loose	
6	1.45		Ta-d pumice MG	greyish-green	dominated by 1-20	medium gravel, porous grain, loose	
7	0.15		Ta-d pumice CS		dominated by 0.5-2	coarse sand	
8	0.3		Paleosol (silt with gravel)	khaki	0.02	hard	

Depth (m): 0 – 4.0. UCS axis: 0, 100, 200

Legend: humus | pumice | volcanic ash | silt | silt with gravel | coarse sand

Fig. 4.2 Vertical stratigraphic columns of the main scarp (**a**) and the right flank (**b**) in the Sakuraoka landslide

Figure 4.3 shows the vertical stratigraphic sections of several points along the survey lines A-A′ and B-B′. In Section -3, the Ta-d pumice is spread on the top with a thickness of approximately 0.05 m, and the middle layer is composed of a mix of crushed pumice and paleosol with a thickness of 0.05 m. The nethermost layer is the off-white and khaki hard paleosol. The soil structures of sections -4, -5, and -6 are almost identical, and both comprise the thin pumice layer at the top and the strong and hard paleosol layer at the bottom. Section -7 was a profile after the excavation of a buried road near the deposition area. It is inferred that there is no downward erosion during the landslide motion, as the excavated road is sound and the soil integrity is not disrupted. The soil structure of section -7 closely matches the main scarp and the right flank, and the Ta-d pumice is located at the bottom.
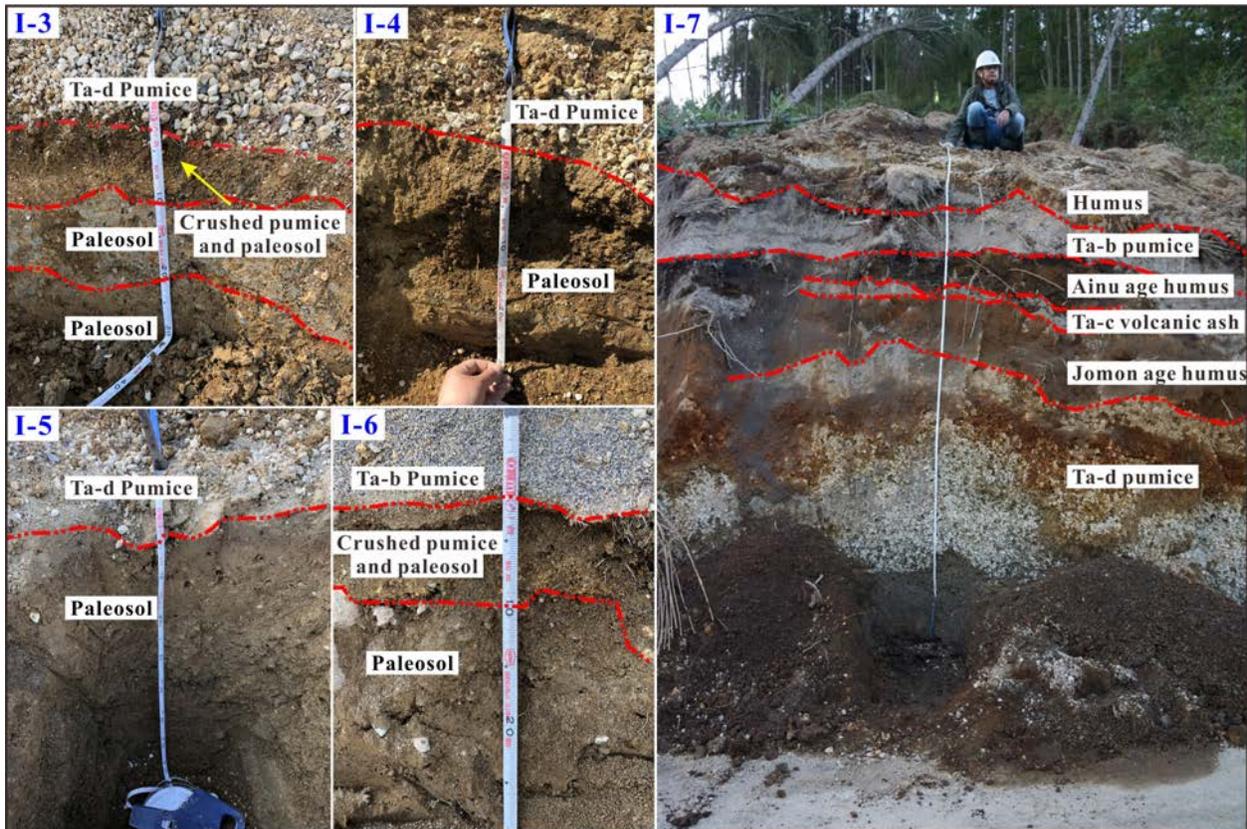
Fig. 4.3 Vertical stratigraphic sections displaying the soil composition of the sliding zone or the sliding mass in the Sakuraoka landslide. The locations of the sections are depicted in Fig. 4.1

Based on the field investigation, the longitudinal sections, and the vertical stratigraphic sections, it is concluded that the Sakuraoka landslide is never a simple collapse of loose pyroclastic fall deposits but rather an integrated motion of the whole pyroclastic fall deposits along the weak layer in Ta-d pumice. The strong ground motion, in combination with the perched groundwater, resulted in the liquefaction in the bottom Ta-d pumice layer and the further motion of whole overlying pyroclastic fall deposits. The scattered pumice remaining on the travel path indicates that the sliding mass was consumed and pinched out.

4.1.2 Gentle debris slide

The Asahi landslide is a typical gentle debris slide, and the general aerial view, as well as the longitudinal sections, are depicted in Fig. 4.4. According to the field reconnaissance and the longitudinal sections (Figs. 4.4b, c), the Asahi landslide is characterized by a planar sliding surface and translational downslope motion. The mean slope angle of the source area along the survey line C-C′ is approximately 14° and the corresponding apparent mobilized friction angle is 7.1°. The mean slope angle of the source area along the survey line D-D′ is approximately 10° and the corresponding apparent mobilized friction angle is 5.2°. The slope steepness of both sub-landslides of the Asahi landslide is lower than that of the Sakuraoka landslide. The most distinguishing difference between the gentle debris slide and the steep debris slide is that the sliding surface in the source area is not exposed. Instead, the wavy humus and pumice were seated on the sliding surface at the source area and the transverse ridges perpendicular to the sliding directions can be easily observed. In the middle of the landslide, an integrated and coherent sliding body can be clearly noticed (Fig. 4.4a). In addition, two distinct segments of the mountain trail can be recognized in Fig. 4.4a. These two segments of the trail are confirmed to be one mountain trail dislocated by the mass displacement, as their widths, trends, and vegetations are nearly identical. Thus, it can be concluded that the sliding mass mobilized as a whole and the integrity, as well as the coherence of the sliding mass, was not largely destroyed. Controlled by the slope steepness, the movement of the sliding mass at the rear stops and remains on the sliding surface.
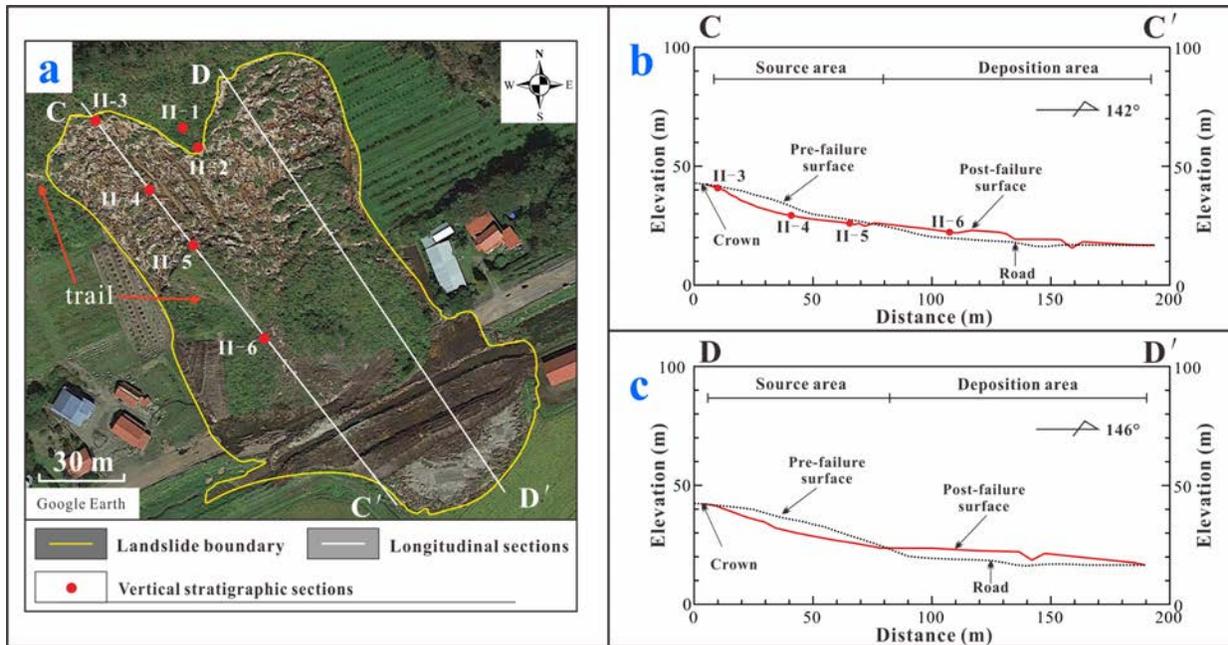
Fig. 4.4 The typical gentle debris slide: Asahi landslide. **a** General aerial view (the base map is derived from the Google Earth). **b** Longitudinal section along survey line C-C′. **c** Longitudinal section along survey line D-D′

Figure 4.5 shows that the composition and structure of sections Ⅱ-2 and Ⅱ-3 are similar to those of the Sakura landslide. The irregular distributed Ta-d pumice MS interlayer can be observed in sections Ⅱ-2 and Ⅱ-3. Sections Ⅱ-4 and Ⅱ-5 show the sliding mass remaining on the sliding surface. The thickness of each pyroclastic fall deposit layer over the paleosol layer is thinner than that of the corresponding layer at the crown, which demonstrates that the sliding mass at the rear was stretched in the downslope motion. Section Ⅱ-6 is located in the stable sliding mass at the deposition area, and the soil structure closely matches that at the crown. This means the integrity of the sliding mass remains unchanged. During the field survey, several concrete pieces of the original road were observed to cross the trench to the landslide toe area. It should be noted that groundwater appeared and perched at a height in the Ta-d pumice layer during the excavation of section Ⅱ-6, and this also happened one day after the excavations of sections Ⅱ-4 and Ⅱ-5. This phenomenon was also observed in the investigation of other landslides. Thus, it can be inferred that the groundwater table was very high and almost reached the exposed sliding surface during

32

the Iburi earthquake. The trench excavations of the Asahi landslide were conducted in May 2019, prior to the rainy season (June, July, and August), while the Iburi earthquake occurred at the beginning of September 2018, just after the rainy season. Therefore, the groundwater table should be very high during the Iburi earthquake, which provides the hydrological condition for the widespread liquefaction during the earthquake.
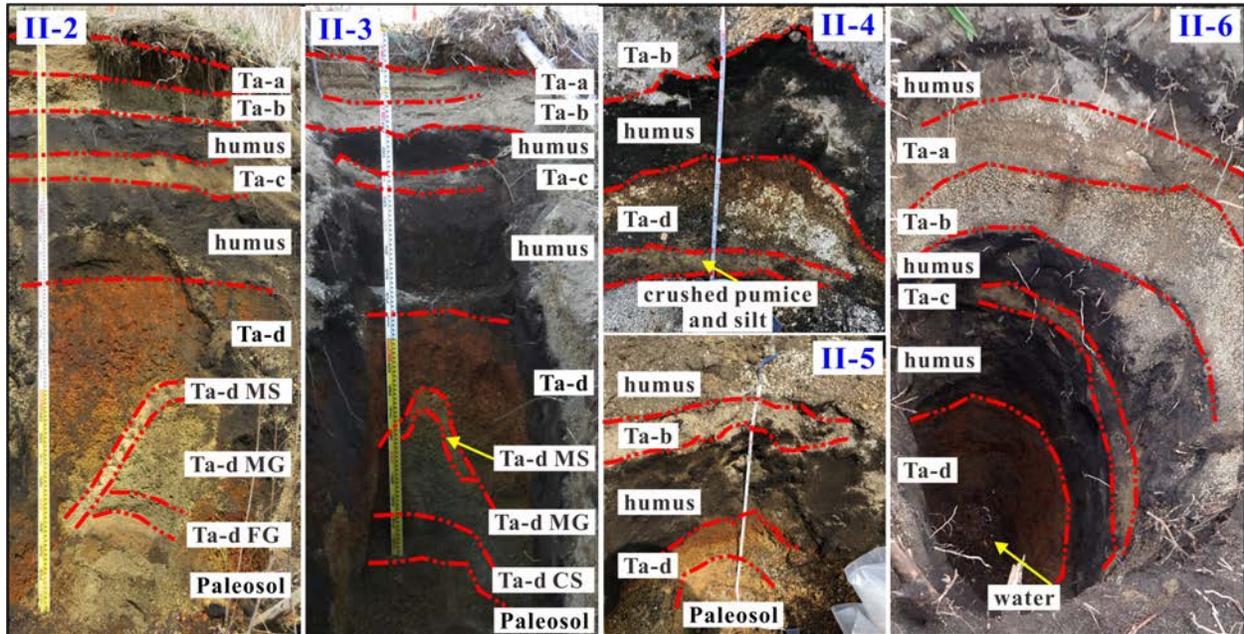
Fig. 4.5 Vertical stratigraphic sections displaying the soil composition of the sliding mass in the Asahi landslide. The locations of the sections are depicted in Fig. 4.4

4.1.3 Cyclic consolidated-undrained triaxial compression tests

The Tomisato-N landslide is a typical mobilization of V-shaped convergent sliding masses occurring in rugged valley terrain. The longitudinal section (Fig. 4.6b) was measured almost along the valley line and the slope angle is approximately 15°. The slope angles of the cross sections (Fig. 4.6c) range from 20° to 40°. This type of landslide constitutes a set of sub-landslides. Clear stripes parallel to the sliding direction can be observed on the exposed sliding surfaces of the sub-landslides. In this light, it is similar to the other two types of

landslides. A series of convergent-sliding sub-landslides provide the provenance and source for the further mobilization in the valley. The disrupted sliding mass along with the stream in the valley forms the flow-like landslide and rushed down to the ditch outlet. A soft disrupted sliding mass could be observed on the travel path, and no integrated sliding block could be discovered in this type of landslide. Several puddles can be observed in the deposition area (Fig. 4.6a). The soil in the deposition area is very soft, and people can be easily trapped, as in swamps. This means the water content and the groundwater table were high during the earthquake.
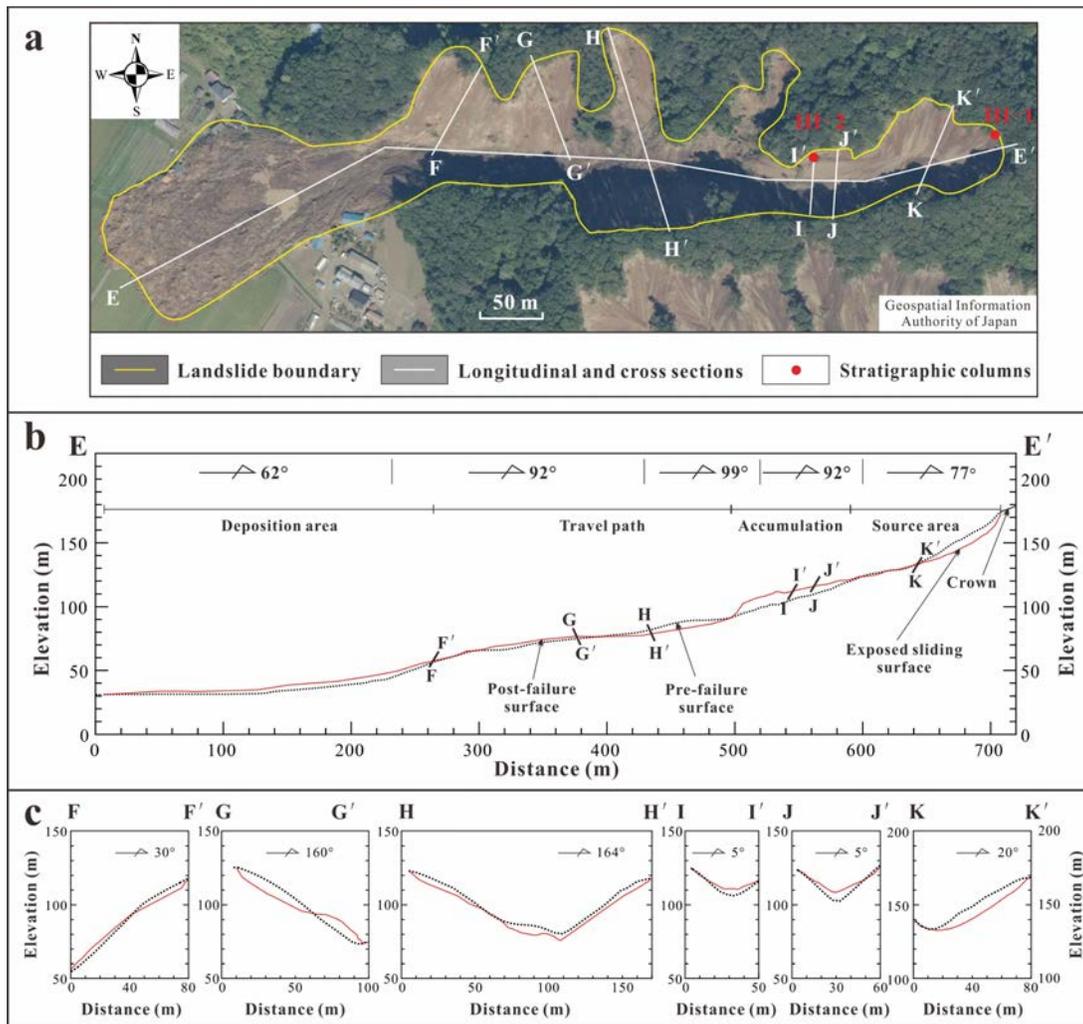
Fig. 4.6 The typical mobilization of V-shaped convergent sliding masses: Tomisato-N landslide. **a** General aerial view (the base map is derived from the Geospatial Information Authority of Japan). **b** Longitudinal section along survey line E-E′. **c** Cross sections

Figure 4.7 shows the vertical stratigraphic sections at the main scarp and the right flank. In the Tomisato-N landslide, the thicknesses of the Ta-a, Ta-b, and Ta-c layers are relatively thin, and the Ta-d pumice comprises the main part of the vertical section. In the right flank, the paleosol layer can be traced to the paleosol layer in the exposed sliding surface, which demonstrates that the sliding surface is localized in the Ta-d pumice layer overlying the stable and hard paleosol layer.

a III-1

NO.	Thickness (m)	Stratigraphy	soil	color	particle size (mm)	others	Uniaxial compressive strength (kPa)
1	0.3		humus				
2	0.3		Ta-b pumice	off-white	dominated by 1-4	loose	
3	0.1		Ainu age humus	black	fine	batt-like, loose	
4	0.3			brown	fine	loose	
5	0.05		Ta-c volcanic ash	off-white	1	loose	
6	0.25		Jomon age humus	dark gray	fine	loose	
7	0.6		Ta-d pumice with volcanic ash	brownish-red	dominated by 0.02-20	pumice with volcanic ash, porous grain	
8	0.1		Ta-d pumice MS		0.3	medium sandy pumice, soft	
9	0.5		Ta-d pumice MG	greyish-green	dominated by 1-20	medium gravel, porous grain	
10	0.05		Ta-d pumice MS		0.3	medium sandy pumice, soft	598
11			Paleosol (silt)	khaki	0.02	hard	

Depth (m): 0, 0.5, 1.0, 1.5, 2.0, 2.5, 2.65
Uniaxial compressive strength scale: 0 100 200 300

b III-2

NO.	Thickness (m)	Stratigraphy	soil name	color	particle size (mm)	others	Uniaxial compressive strength (kPa)
1	0.1		humus				
2	0.1		Ta-b pumice	off-white			
3	0.1			black	fine		
4	0.55		Jomon age humus	brown	middle-sandy humus	loose	
5	0.5		Ta-d pumice with volcanic ash	brownish-red	dominated by 0.02-20	pumice with volcanic ash, porous grain, loose	
6	0.5		Ta-d pumice MG	greyish-green	dominated by 1-20	medium gravel, porous grain	
7	0.1		Ta-d pumice MS		0.3	medium sandy pumice, soft	
8	0.03					soft	
9			Paleosol (silt)	khaki	0.02	hard	

Depth (m): 0, 0.5, 1.0, 1.5, 2.0, 2.15
Uniaxial compressive strength scale: 0 100 200 300 400 500

Legend: humus | pumice | volcanic ash | silt

Fig. 4.7 Vertical stratigraphic columns of the main scarp (**a**) and the right flank (**b**) in Tomisato-N landslide

4.1.4 Summarization of the failure mode

In this section, three main types of the coseismic landslides were classified and their failure modes were described in detail. Generally, localized liquefaction occurs in the weak layer of the Ta-d pumice during the strong ground motion, and the integrated sliding failure occurs in the initiation stage. Then, the whole sliding mass mantled on the liquefied layer moves downslope. In the motion stage, three mobilization types (steep debris slide, gentle debris slide, and the mobilization of V-shaped convergent sliding masses) appear controlled by the topography and other factors. These types cover the majority of the Iburi landslides. Besides, the combination of multiple motion styles also registers a large number of Iburi landslides.

4.2 Geotechnical properties

The soil composition of the landslides is one of the predominant factors controlling the landslide occurrence; it is important to understand the soil property to investigate the failure mechanism of the landslides (Gratchev and Towhata 2010; Wiemer et al. 2015). To investigate the geotechnical properties of the soil layers, a set of in-situ and laboratory tests were conducted. The undisturbed samples applied in the tests were taken from the main scarp of the Asahi landslide. The in-situ density, dry density, water content, specific gravity, void ratio, and degree of saturation were obtained.

The test results are summarized in Table 4.1. As the specific gravities of different pumice particles vary with the grain size, porosity, and structure, the specific gravities of pumice layers in Table 4.1 were the results of the triturated samples. In fact, the specific gravities of some pumice samples are smaller than 1. As illustrated in Table 4.1, the degrees of saturation of the paleosol (silt) and the Ta-d pumice MS are very high, and the water content of the Ta-d pumice MS is very high as well. The dry densities of the Ta-d pumice layers are relatively low due to their large porosity. These tested parameters are necessary for soil classification and the preparation of remolded samples in the triaxial tests.

Table 4.1 Physical properties of the soil samples from the crown of the Asahi landslide

Soil layer	ρ (kg/m3)	ρ_d (kg/m3)	w (%)	G_s	e	S_r (%)
Surface humus	1,258	1,083	16.2	2.653	1.451	29.7
Ta-a pumice	1,249	1,065	17.2	2.733	1.565	30.1
Ta-b pumice	909	693	31.2	2.641	2.813	29.3
Black humus	1,083	540	101	2.528	3.684	69.1
Ta-c pumice	1,333	1,086	22.8	2.769	1.550	40.8
Ta-d pumice with volcanic ash	1,122	506	121	2.553	4.041	76.7
Ta-d pumice MG	874	281	210	2.542	8.029	66.6
Ta-d pumice FG	891	530	68.1	2.624	3.950	45.2
Ta-d pumice CS	1,023	511	100	2.627	4.141	63.6
Ta-d pumice MS	1,177	385	206	2.631	5.842	92.8
Paleosol (silt)	1,649	1,028	60.4	2.735	1.660	99.5

Considering most Iburi landslides are integrated sliding along the interface between the Ta-d pumice and the hard paleosol, soils located around the sliding zone (i.e., the Ta-d pumice layers and the paleosol layer) are regarded as the main objectives. Figure 4.8 shows the grain size distributions of the soils from the main scarp of the Asahi landslide. The Ta-d pumice FG and the Ta-d pumice CS are taken from the vertical sections   -2 and   -3 (Fig. 4.4a), respectively. Although these two samples are from the same soil layer at different localities, their grain-size distributions have significant differences. The fine-sized particle (less than 0.075 mm) of the Ta-d pumice CS is high and the grain strength of the Ta-d pumice CS is much lower than that of the Ta-d pumice FG. The Ta-d pumice MS and the paleosol (silt) layer contain not only high fine-sized particles but also low coarse-sized particles. Thus, the uniformity coefficients (C_u) for these two layers are large and the coefficients of curvature (C_c) are small (Table 4.2). The paleosol layer is abundant in clay and fine-sized particles, and the clay and fine-sized contents are as high as approximately 35% and more than 60%, respectively. While the dry density is small, this paleosol layer maintains a low permeability. The content of the Ta-d pumice MS is dominant by medium sand, and large amounts of unbreakable black sand from the pumice are

retained inside. Besides, the Ta-d pumice MS contains small amounts of unbroken pumice particles and the strength of these particles is very low.
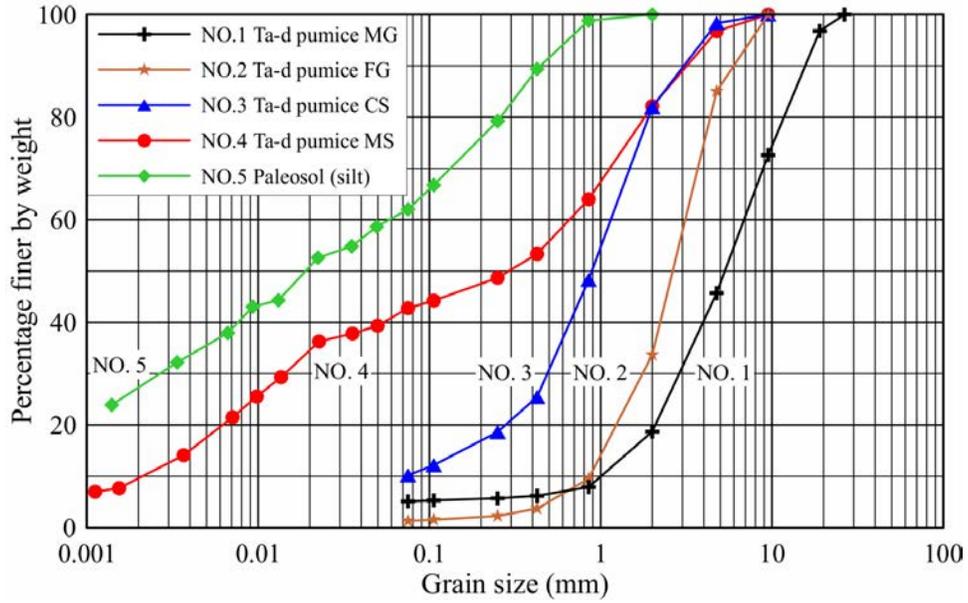
Fig. 4.8 Grain size distributions of the samples from the main scarp (II-2 and II-3 in Fig. 4.4) of the Asahi landslide

Table 4.2 Grain size distributions of the samples around the sliding surface

	Layer name	D_{50} (mm)	C_u	C_c
No.1	Ta-d pumice MG	5.2	6.9	1.1
No.2	Ta-d pumice FG	2.4	3.6	1.1
No.3	Ta-d pumice CS	0.89	15	3.0
No.4	Ta-d pumice MS	0.29	3.0×10^2	0.13
No.5	Paleosol (silt)	0.019	1.2×10^2	0.21

39

4.3 Static consolidated-undrained triaxial compression tests

Figure 4.9 shows the stress-strain relationships of the saturated specimens in the consolidated undrained tests, and only the test results with confining stress of 40 kPa were depicted. The general trends of the axial stress increment and the pore water pressure of Ta-d pumice MG (No. 1 in Figure 4.9) and Ta-d pumice FG (No. 2 in Figure 4.9) are similar. The pore water pressures of both specimens increase rapidly with an increase in the axial strain, and the specimens are mainly compacted at this stage. When the axial strain reaches approximately 3%, the pore water pressure reaches a peak value and the increment of the pore water pressure is larger than 1/3 of the axial strain increment. This means excess pore water pressure is generated at this stage (Skempton 1954; Ortigao et al. 1995). Then, with the continuous increase of the axial strain, the specimen changes from a contraction state to a dilation state to overcome the bite force between particles, and the pore water pressure decreases accordingly. The axial stress increment increases with an increase in the axial strain to a large value, indicating the strain hardening of the two types of pumice specimens.
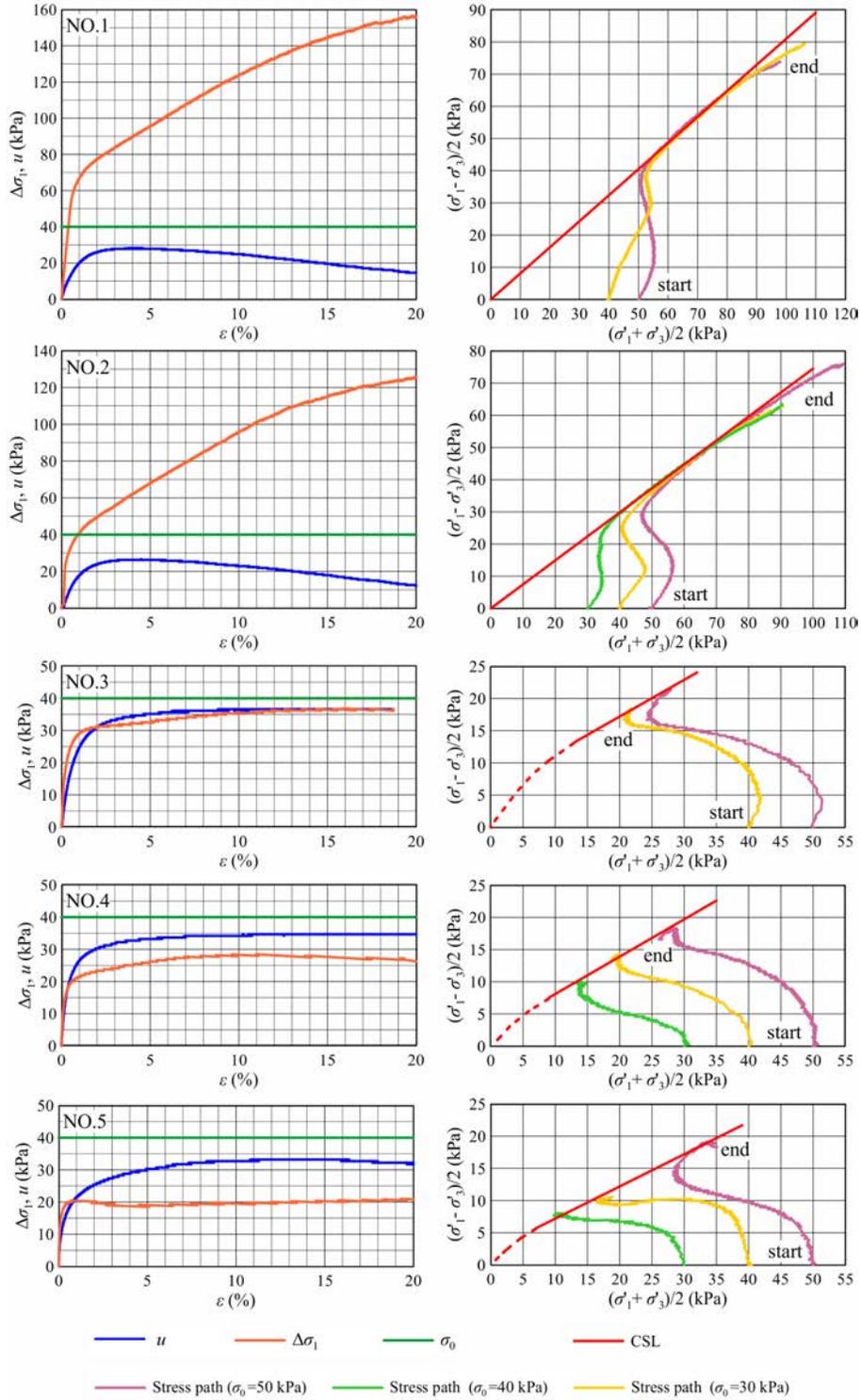
Fig. 4.9 Stress–strain relationships under the confining pressures of 40 kPa (left) and effective stress paths (right) of the saturated specimens in the consolidated-undrained triaxial compression tests

The behavior of the Ta-d pumice CS (No. 3 in Figure 4.9) in the consolidated-undrained triaxial tests is quite different from those of the Ta-d pumice MG and the Ta-d pumice FG. The axial stress increment and the pore water pressure increase with an increase in the axial strain and then remain stable. The only contraction appears for the Ta-d pumice CS. The peak value of the axial stress increment is 36.4 kPa, which is far less than the peak values of the Ta-d pumice MG and the Ta-d pumice FG. This phenomenon results from the specimen particle being crushed under increased axial strain. To justify the occurrence of grain crushing, grain size analysis of the Ta-d pumice FG and the Ta-d pumice CS after the test was conducted as well. As depicted in Fig. 4.10, the grain size distribution curve of the Ta-d pumice FG after the test is similar to before test, while the grain size distribution curve of the Ta-d pumice CS after the test deviates remarkably to the left. The considerable increase in the fine particles (left deviation) of the Ta-d pumice CS indicates that grain crushing must have occurred during the compression tests. Figure 4.11 shows the stress-strain relationship and effective stress path of the remolded specimen from the Ta-d pumice FG. The grain size distribution of the remolded specimen was conditioned to be consistent with that of the Ta-d pumice CS. The general trends of the axial stress increment and the pore water pressure of the remolded specimen are similar to those of the Ta-d pumice FG, but the peak value of the axial stress is smaller. Thus, the grain crushing phenomenon is considered to control the stress-strain behavior of Ta-d pumice CS. The grain crushing inhibits the occurrence of dilation and strain hardening.
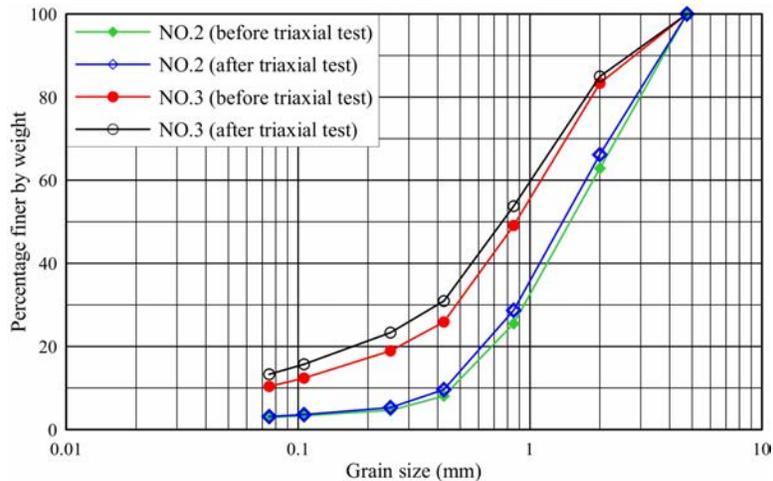
Fig. 4.10 Grain size distributions of two specimens before and after the triaxial test
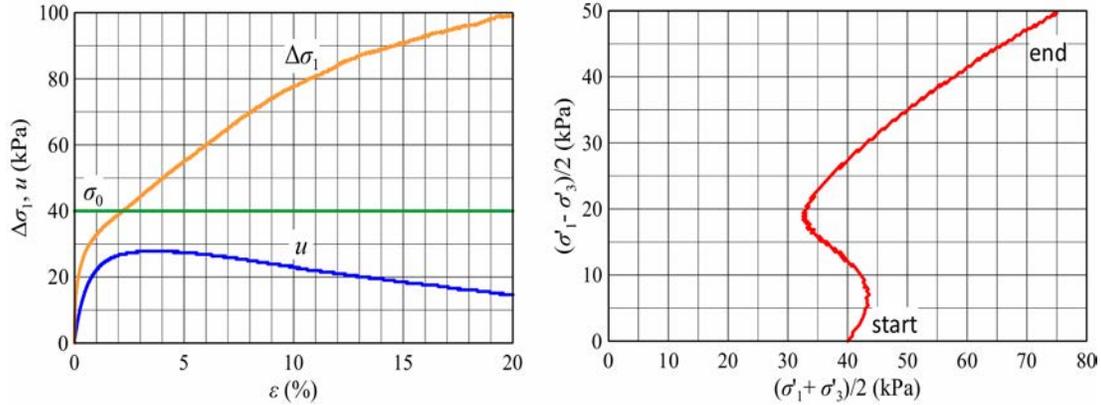
Fig. 4.11 Stress-strain relationship under the confining pressures of 40 kPa (left) and effective stress path (right) of the remolded specimen from Ta-d pumice FG; the grain size distribution of the remolded specimen was conditioned to be consistent with that of the Ta-d pumice CS

The axial stress increment of the Ta-d pumice MS (No. 4 in Figure 4.9) first increases with an increase in the axial strain and then decreases. The peak axial stress increment is 28.4 kPa. The axial stress increment of the paleosol specimen (No. 5 in Figure 4.9) reaches its peak when the axial strain is approximately 1%, while the pore water pressure is still slowly increasing. The pore water pressures of the Ta-d pumice CS, the Ta-d pumice MS, and the paleosol approximate the confining stress, indicating that static liquefaction occurs in all these specimens. However, the pore water pressure of the Ta-d pumice MS clearly increases much faster than that of the paleosol specimens. This phenomenon can be also observed in cyclic triaxial compression tests. Thus, it could be concluded that the Ta-d pumice MS is more susceptible to liquefaction.

In consolidated-undrained triaxial compression tests, the cohesion of the remolded specimens with normal consolidation is positively correlated with the consolidation pressure, and the critical state line (CSL) passes through the origin in general. In this section, the shear strengths of specimens under different confining pressures were obtained (Fig. 4.9). The cohesion and the friction angle were not severally calculated, as they are difficult to clearly separate (Li 2004). The equations for the CSL and the shear strength of the five layers are summarized in Table 4.3. The shear strength of both the paleosol layer and the Ta-d pumice layers is high, which explains why the pumice slope can remain stable in a natural state while the cohesion of the loose pumice

is very low. The static shear strength of the five layers is positively correlated with the grain size, i.e., the shear strength of the Ta-d pumice MG is the largest while the shear strength of the Ta-d pumice MS and the paleosol is relatively low. The effective stress paths of the Ta-d pumice MG and the Ta-d pumice FG move toward the upper-right side along the CSL after reaching the CSL. This implies that strain hardening occurs in these specimens. The effective stress path of the Ta-d pumice MS shows a lower-left trend after reaching the CSL.

Table 4.3 CSL equations and failure criterion equations of the samples summarized from the consolidated-undrained triaxial compression tests

	Layer name	CSL equation	Failure criterion equation
No.1	Ta-d pumice MG	$y = 0.81\,x$	$\tau' = 1.38\,\sigma'$
No.2	Ta-d pumice FG	$y = 0.75\,x$	$\tau' = 1.13\,\sigma'$
No.3	Ta-d pumice CS	$y = 0.57\,x + 5.8$	$\tau' = 0.69\,\sigma' + 7.06$
No.4	Ta-d pumice MS	$y = 0.58\,x + 2$	$\tau' = 0.71\,\sigma' + 2.46$
No.5	Paleosol (silt)	$y = 0.50\,x + 2.2$	$\tau' = 0.58\,\sigma' + 2.54$

4.4 Cyclic consolidated-undrained triaxial compression tests

Soil liquefaction resulting from strong ground motion has been an important topic in geotechnical earthquake engineering since the concentrated research on the soil liquefaction in the 1964 Alaska and Niigata earthquake (Fukuoka 1966; Seed 1968; Scott and Zuckerman 1972; Takch et al. 2016). Shallow slope failures triggered by strong earthquakes are commonly related to cyclic liquefaction in soil (Seed 1968; Ishihara et al. 1990; Harp et al. 2003; Pei et al. 2017). To study the anti-liquefaction strength of the soils around the sliding zone under seismic loading, a set of cyclic triaxial (CTX) strain-controlled tests were performed. The corrected pore water pressure ratio is defined in Eq. 1. The confining stress applied in the CTX test is 40 kPa.

The variation curves of the axial stress increment, the axial strain increment, and the pore water pressure ratio with the number of loading cycles of Ta-d pumice CS are illustrated in Fig. 4.12. As the number of loading cycle increases, the ability to resist loading gradually decreases. Thus,

the amplitude of the axial stress variation reduces and stabilizes at a relatively low value finally. The amplitude of the axial strain variation increases with an increase in the number of loading cycles. The pore water pressure varies with the cyclic loading, and excess pore water pressure is generated. The excess pore water pressure rises continuously and approximates the confining stress. Thus, liquefaction occurs in the Ta-d pumice CS specimen. The effective stress paths (Fig. 4.13) presents the cyclic mobility behavior of Ta-d pumice CS in the CTX test. The pore water pressure rapidly increases initially and reaches a stable state in the following cycles.

The correlation between the cyclic shear stress ratio ($\frac{\tau_d}{\sigma_0'}$) and the logarithm of N_L ($\lg N_L$) of all samples are shown in Fig. 4.14. The liquefaction resistance of the four soil layers is further concluded as follows: Ta-d pumice MS < Ta-d pumice CS < Paleosol (silt) < Ta-d pumice FG.
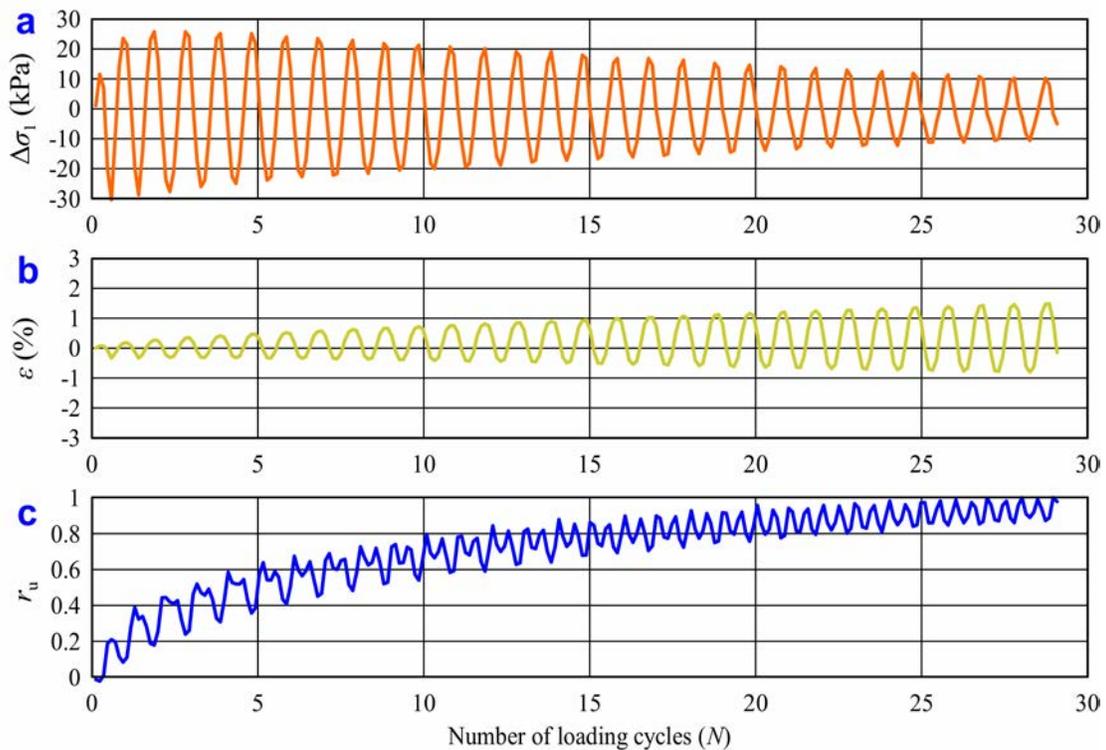
Fig. 4.12 Correlations between the axial stress increment ($\Delta\sigma_1$) (**a**), the axial strain increment (ε) (**b**) and the pore pressure ratio (r_u) (**c**) with the number of loading cycles (N) of Ta-d pumice CS
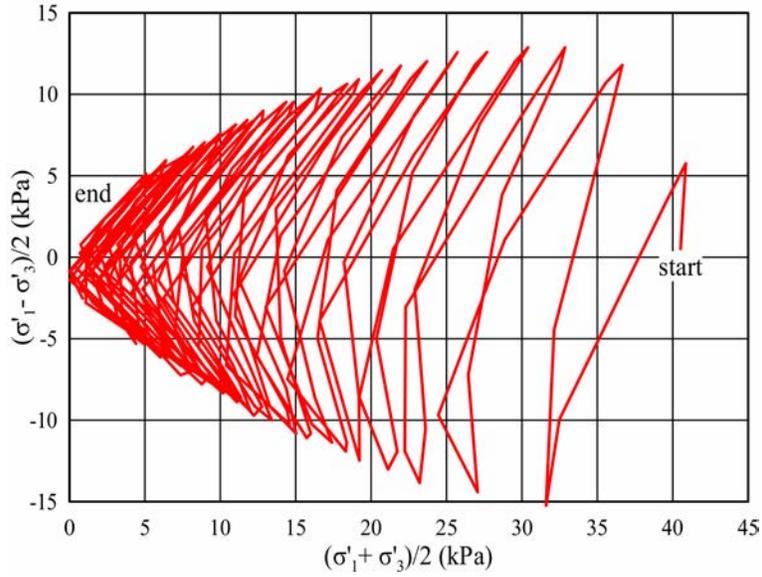
Fig. 4.13 Effective stress path of Ta-d pumice CS during the consolidated-undrained cyclic loading triaxial test
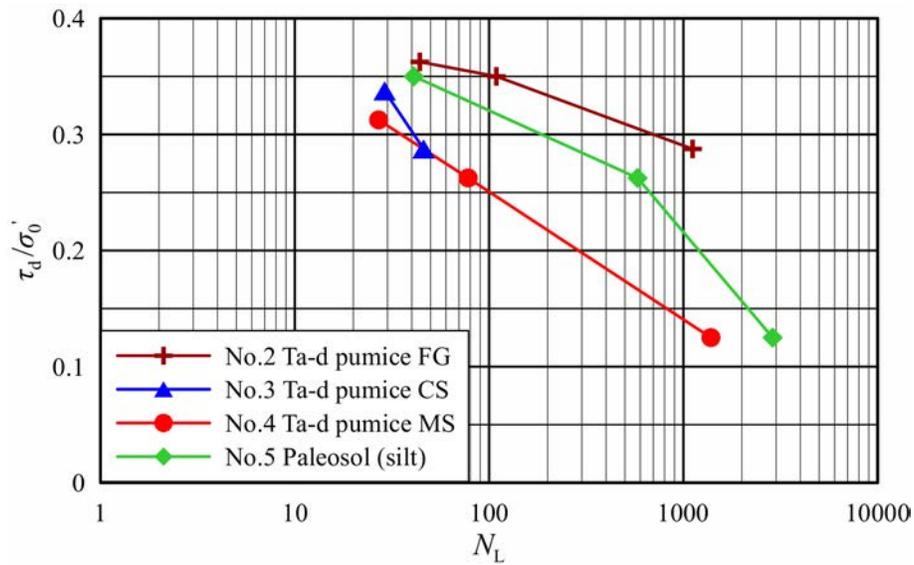
Fig. 4.14 Correlations between the cyclic shear stress ratio $(\frac{\tau_d}{\sigma_0'})$ and the number of cycles required for liquefaction (N_L)

Field survey and test results of Kataragal landslide

5.1 Features of the Kataragai landslide

As is depicted in Fig. 5.1, the Kataragai landslide is characterized by a wide source area, a narrow travel channel, and a spread deposition area. Three ponds can be observed at the crown, and one pond (pond 4 in Fig. 5.1) was located in the slope before the slope failure. During the fieldwork, scattered dead fishes (Fig. 5.2d) were spotted, which demonstrates that perennial water must have been impounded in the ponds. The source area of the Kataragai landslide is composed of two sub-landslides. A pre-existent scarp with a height of 1.0-2.0 m was located in the slope before the slope failure (Fig. 5.1). In the source area, the left flank ran parallel to the pre-existent scarp. The soil with a thickness of approximately 0.5 m at the pre-existent scarp survived. It is inferred that the strength of the soil increased as the steep surface of the pre-existent scarp became dry fast and the moisture content decreased. In the deposition area, the sliding mass moved within the pre-existent scarp. The source area and the deposition area are boarded on the pre-existent scarp and the motion modes in the source area and the deposition area are distinctly different. In the source area, the landslide moved in a disrupted state, and disrupted sliding mass could be observed in the source area (Fig. 5.2a). After running across the pre-existent scarp and destroying the pond, the mobilization mode changed to flow-like state due to the entrainment of the water impounded in the pond 4. The soil in the deposition area is very soft and fully saturated, and people can be easily trapped as in swamps. Finally, the sliding mass spread in the flat area around the road, and part of the sliding mass ran across the guardrail to the river.
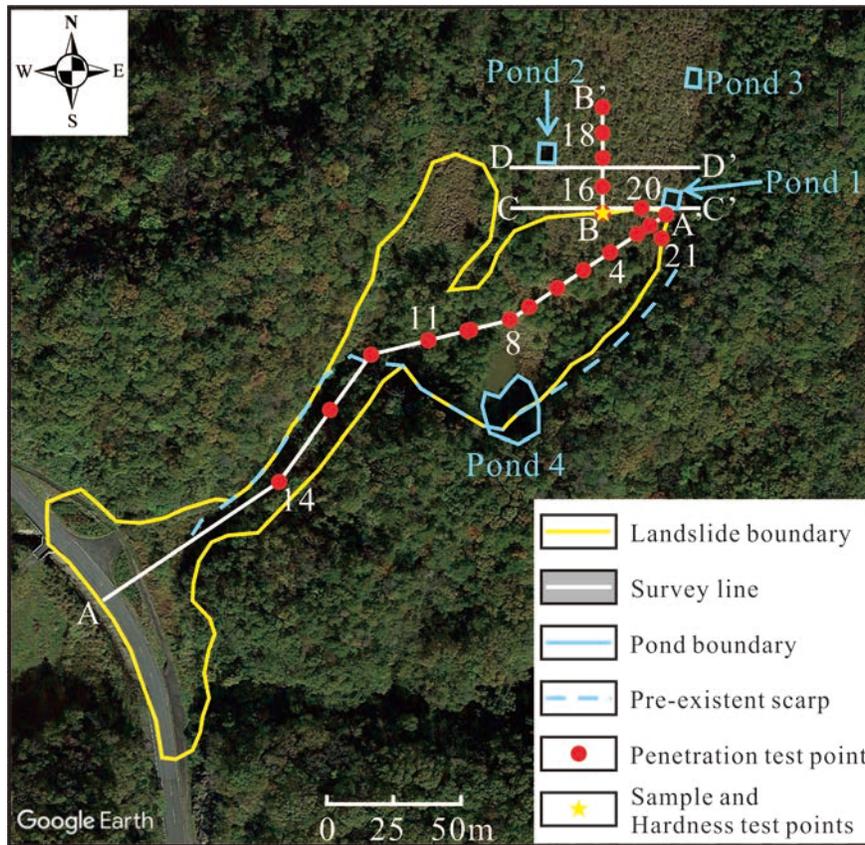
Fig. 5.1 General aerial view of the Kataragai landslide. The base map is derived from the Google Earth

Fig. 5.2 Photographs of the Kataragai landslide. **a** Source area. **b** Deposition area. **c** General view of pond 1. **d** Dead fish scattered in the slope

Figure 5.3 is the longitudinal section along the survey line A-A′. The post-failure surface was measured in the field and the pre-failure surface was generated from a 5×5 m DEM. The longitudinal section shows the Kataragai landslide occurred on the gentle slope with a slope angle of approximately 7°, which is much lower than the slope angles of the adjacent area. The apparent friction angle of the Kataragai landslide is approximately 6.8°. The location of the sliding surface was determined by the portable penetration test along the survey line A-A′ (Fig. 5.4).
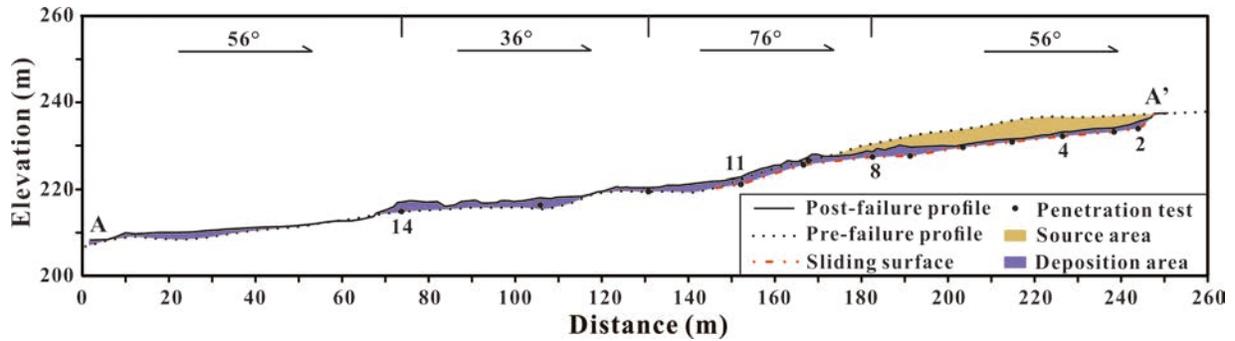
Fig. 5.3 Longitudinal section of the Kataragai landslide along survey line A-A′
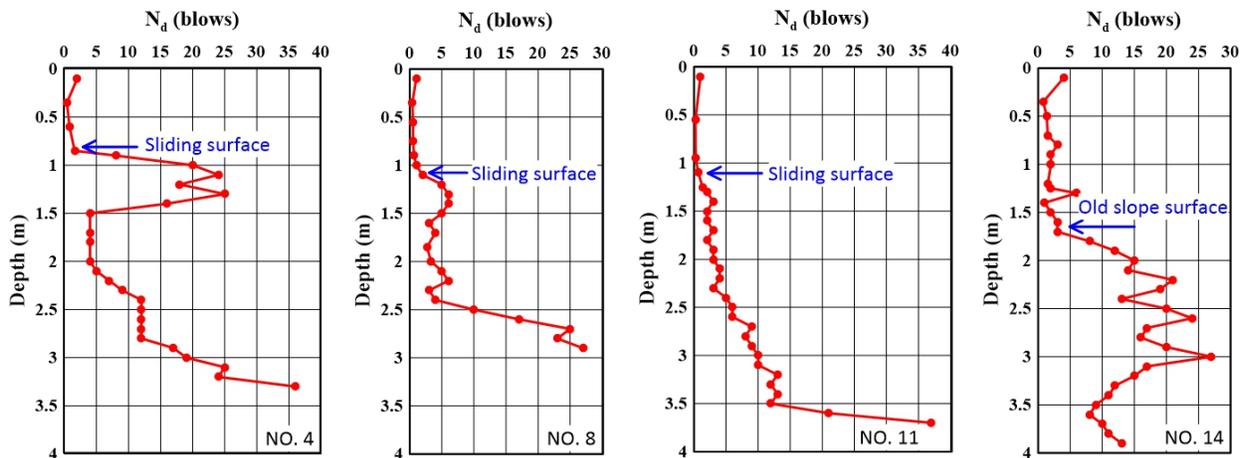
Fig. 5.4 Portable dynamic cone penetration test results of representative points along survey line A-A′

5.2 Physical properties

A vertical section displaying the soil composition of the main scarp is depicted in Fig. 5.5b. As the Kataragai landslide occurred in an artificial slope refilled after the clay mining, the soil composition is relatively homogeneous. The soil is mainly composed of the medium sand with gravel, and the gravel is characterized by fine psephicity. Based on the hardness test, the uniaxial compressive strength evidently decreases in a sandy layer with a depth of approximately 1.9 m (Fig. 5.5a). It was observed that the seepage flowed out in this sandy layer and the groundwater appeared and perched at the bottom of this section a while after the excavation of the vertical

section (Fig. 5.5c, d). The groundwater table of the Kataragai landslide almost approaches to the post-failure ground surface. The results of the penetration test conducted at the main scarp also indicate that the soil strength reaches a low value at a depth between 1.5 m and 2.0 m (Fig. 5.6). The critical value of portable dynamic cone penetration test blow count for liquefaction evaluation varying with depth can be calculated by Equation 3.3. In this work, only the liquefaction potential triggered by the Western Shimane earthquake is considered. Based on the distribution map of the PGA in Fig. 2, the Kataragai landslide is located in the area with a PGA between 4.0 m/s2 and 4.5 m/s2. Thus, a N0 value of 19 was selected. Based on the monitoring data of two stations proximal to the Kataragai landslide, the period of the ground acceleration is between 0.2 s and 0.44 s and the average period is 0.26 s (National Research Institute for Earth Science and Disaster Resilience (NIED) 2019). Considering that the period of the ground acceleration is short, β is selected as 0.80. The green lines in Figure 5.6 indicate the critical lines. Most blow counts of the penetration test points with the depth of 1.5-2.0 m at the main scarp are less than the critical line, which demonstrates that the soil layer with a depth of 1.5-2.0 m is susceptible to liquefaction. The penetration test was also conducted along survey line B-B′ at the crown and the distance between the measuring points is 10 m (Fig. 5.7). The results show that the weak layer at the crown gradually descends from 1.5-2.0 m to 2.0-3.0 m. Moreover, the depth of the groundwater was also obtained through the penetration test, and the depth graduates from 1.9 m to 0.4 m along survey line B-B′. This means the groundwater table maintained a high level before the slope failure, and then decreased to a low level due to the exposure of the main scarp after the landslide occurrence.
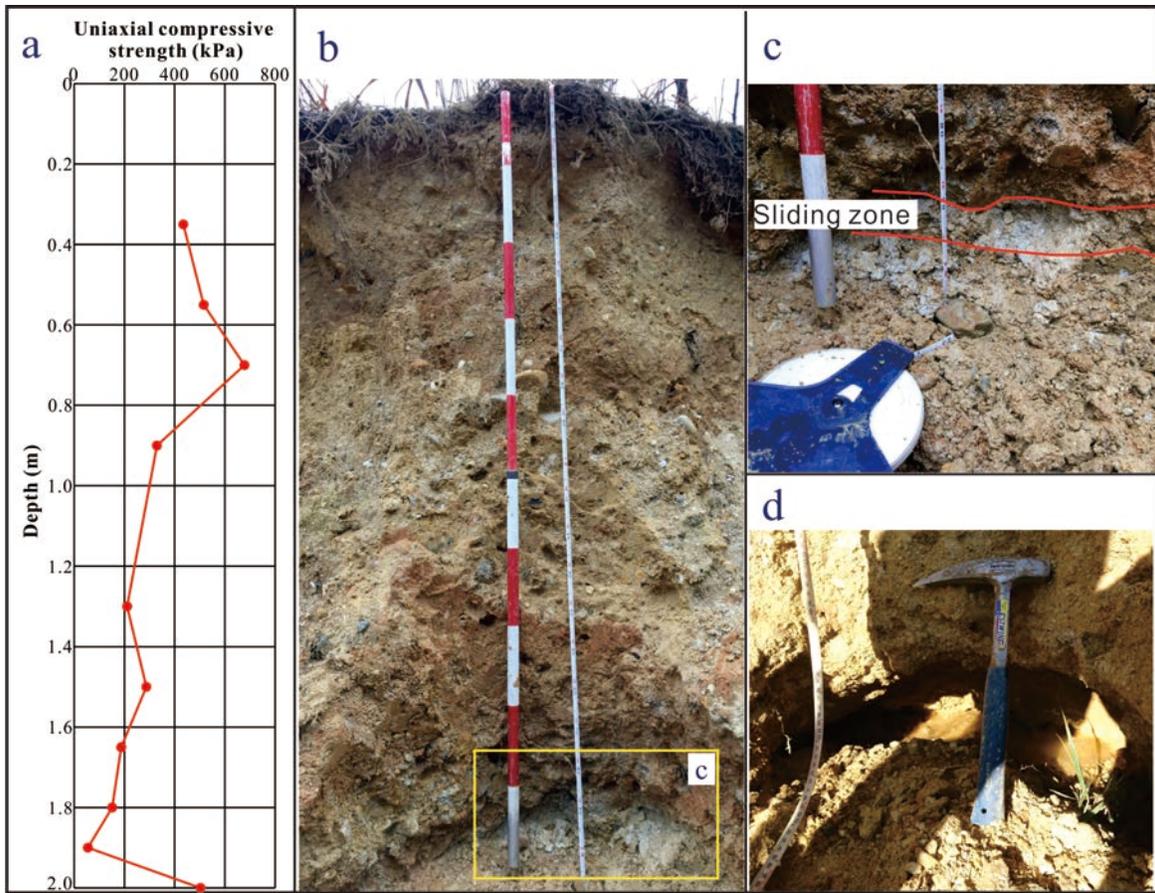
Fig. 5.5 Vertical section and hardness test result of point B at the main scarp. **a** Hardness test result. **b** Vertical section. **c** Sliding zone. **d** Groundwater leakage
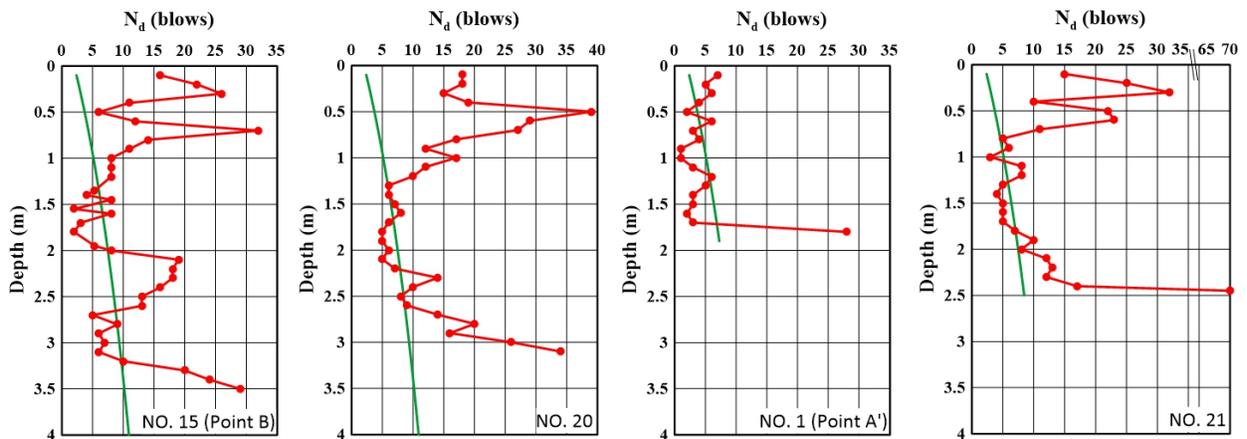
Fig. 5.6 Result of the portable dynamic cone penetration test at the main scarp
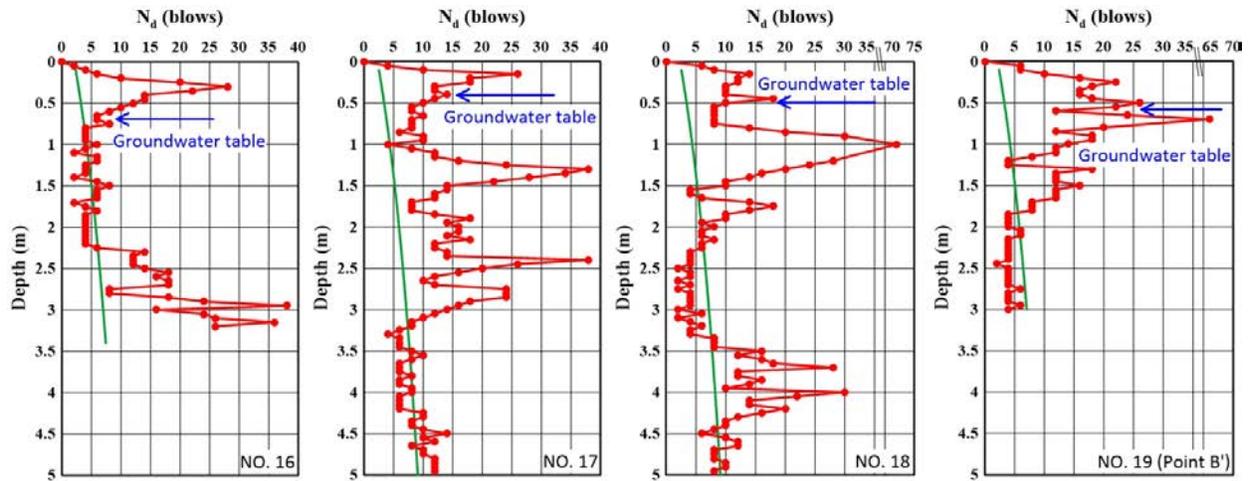
Fig. 5.7 Results of the portable dynamic cone penetration test at the crown along survey line B-B′

Table 5.1 is a list of the physical properties of soil with different depth at the main scarp (point B in Fig. 5.1). The tested soil parameters include in-situ density(ρ), dry density(ρ_d), water content (w), specific gravity (Gs), void ratio (e), and degree of saturation (S). Clearly, the soil layers with the depth lower than 1.9 m are almost fully saturated. The dry density of the soil decreases firstly and then increases from top to bottom. The minimum dry density appears at the sliding zone with a depth of 1.9 m.

Table 5.1 Physical properties of the soil samples from point B

No.	Depth (m)	ρ (kg/m^3)	ρ_d (kg/m^3)	w (%)	G_s	e	S_r (%)
1	0.3	1,897	1,678	13.1	2.612	0.556	61.5
2	0.6	1,711	1,510	13.3	2.611	0.729	47.6
3	0.9	1,834	1,579	16.2	2.613	0.655	64.4
4	1.3	1,793	1,469	22.1	2.663	0.813	72.3
5	1.6	1,804	1,473	22.5	2.667	0.811	73.9
6	1.9	1,902	1,451	31.1	2.655	0.830	99.5
7	2.0	2,049	1,681	21.9	2.666	0.586	99.6

In this work, the specimens at the depths of 1.6 m, 1.9 m, and 2.0 m, were used in the grain size analysis. The grain size distributions of the specimens are illustrated in Fig. 5.8. The contents of the fine-sized particle (less than 0.075 mm) at the depths of 1.6 m and 2.0 m are almost identical, while the fine content of specimen at the depth of 1.9 m (sliding zone) is relatively low. Based on the uniformity coefficient (C_u) and the coefficients of curvature (C_c) of the specimens in Table 5.2, it can be concluded that the soils at the depths of 1.6 m and 2.0 are characterized by good gradation and low permeability, while the soil at a depth of 1.9 m is characterized by poor gradation and high permeability.
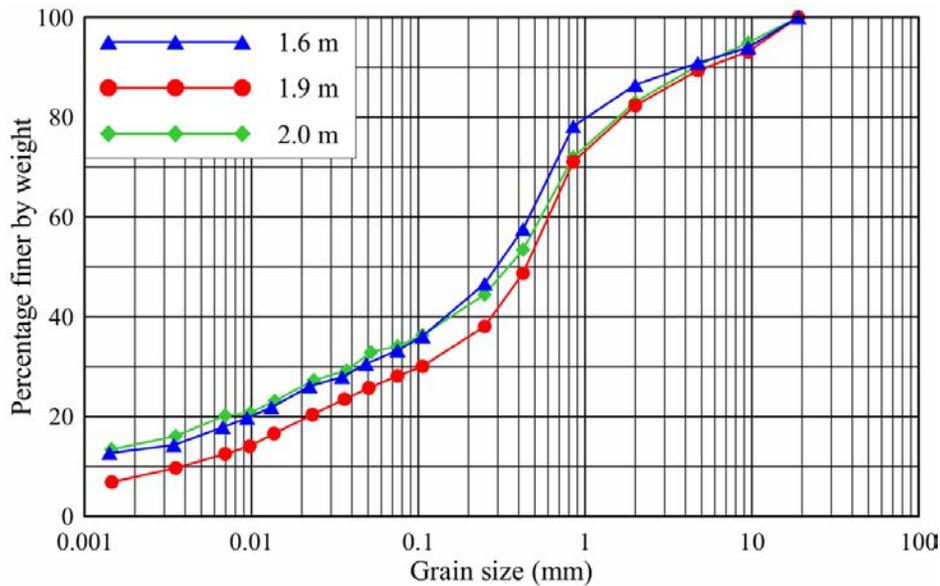
Fig. 5.8 Grain size distributions of the specimens from point B

Table 5.2 Grain size distributions of the soils around the sliding surface

No.	Depth (m)	D_{50} (mm)	C_u	C_c
1	1.6	0.34	4.2×10^2	2.3
2	1.9	0.44	1.6×10^2	5.1
3	2.0	0.29	3.5×10^2	2.0

5.3 Shear behavior and anti-liquefaction strength

To investigate the shear behavior and anti-liquefaction strength, the static and cyclic triaxial tests were conducted on the specimens around the sliding zone. Three specimens with depths of 1.6 m, 1.9 m, and 2.0m were selected. The variation curves of the axial stress increment ($\Delta\sigma=\sigma_1-\sigma_0$) and the pore water pressure (u) with the axial strain (ε) in the static consolidated-undrained triaxial compression test were illustrated in Fig. 5.9. Only test results with the consolidation pressures of 40kPa were displayed in this work. The variation tendencies of $\Delta\sigma$ and u for the three specimens are similar. $\Delta\sigma$ increases with the continuous increase of ε and then reaches a stable state at an axial strain of 17%, which indicates the occurrence of strain hardening. u firstly increases rapidly with an increase in the ε, and the specimen is mainly compacted at this stage. The increment of u is larger than 1/3 of $\Delta\sigma$ at this stage, and excess pore water pressure is generated from the contraction of the specimen at this stage (Skempton 1954; Ortigao et al. 1995). Then, u decreases with the continuous increase in ε and the specimen changes from a contraction state to a dilation state. It should be noted that although the fine contents of the specimens with depths of 1.6 m and 2.0 m are similar, the content of the particle with size between 0.1 mm and 1.0 mm in the specimen that obtained from a depth of 1.6 m is slightly high than that from a depth of 2.0 m, and the density of the specimen from a depth of 1.6 m is far less than that from a depth of 2.0 m. The dilation in the specimen from a depth of 1.6 m is more remarkable than that from a depth of 2.0 m, which means the increase in the content of the "coarser particle" (with size between 0.1 mm and 1.0 mm) may magnify the dilation. The effective stress paths tendencies of all specimens are similar, the effective stress paths move toward the upper-right side along the CSL after reaching the CSL. The shear strength formulas of specimens are listed in Table 5.3.
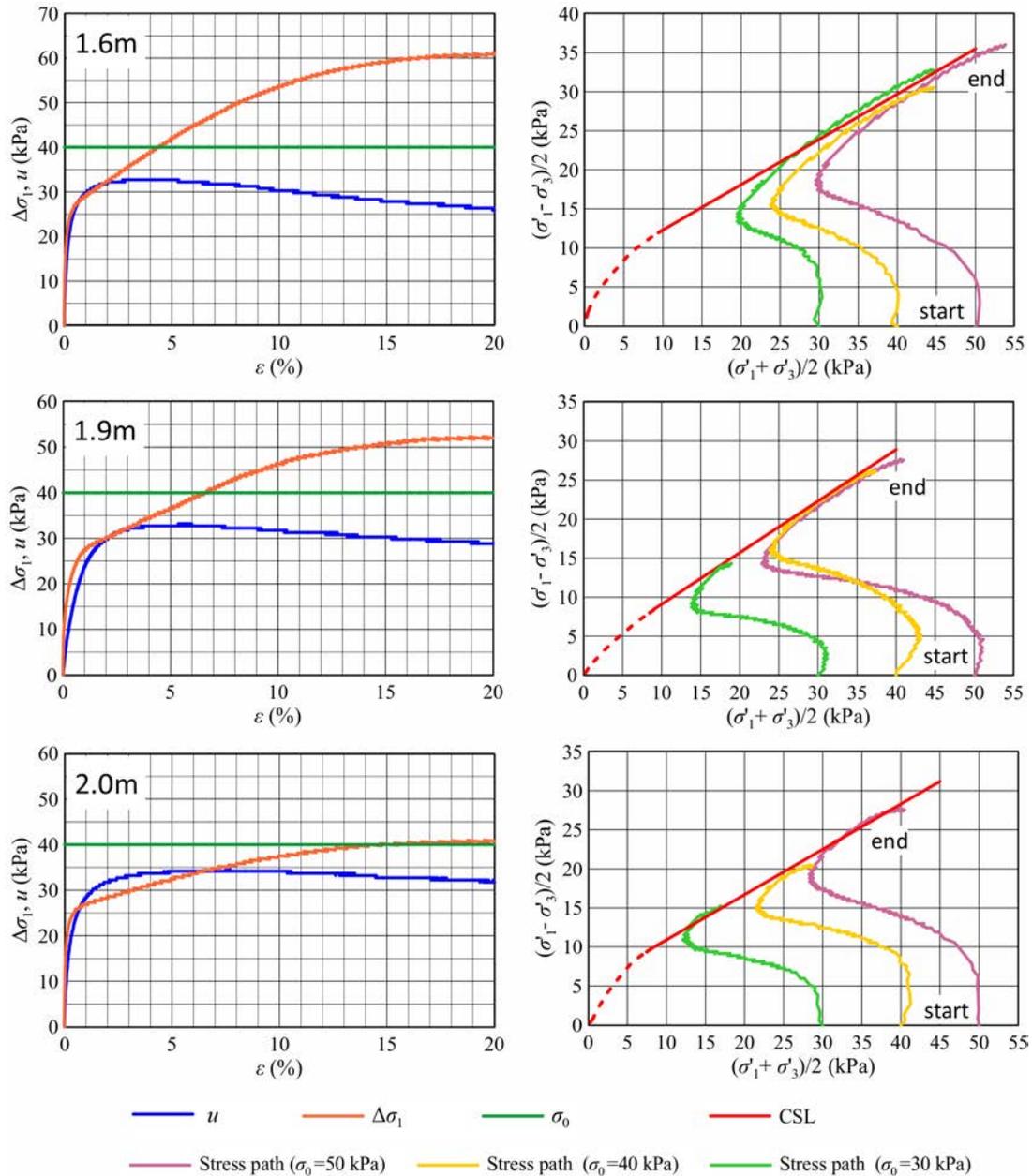
Fig. 5.9 Stress–strain relationships under the confining pressures of 40 kPa (left) and effective stress paths (right) of the saturated specimens in the consolidated-undrained triaxial compression tests

Table 5.3 CSL equations and failure criterion equations of the samples summarized from the consolidated-undrained triaxial compression tests

No.	Depth (m)	CSL equation	Failure criterion equation
1	1.6	$y = 0.58\,x + 6.5$	$\tau' = 0.75\,\sigma' + 8.13$
2	1.9	$y = 0.66\,x + 2.5$	$\tau' = 0.88\,\sigma' + 3.33$
3	2.0	$y = 0.58\,x + 5.1$	$\tau' = 0.71\,\sigma' + 6.26$

In this study, the anti-liquefaction strengths of the specimens with depths of 1.6 m, 1.9 m, and 2.0m were investigated by the cyclic consolidated-undrained triaxial compression test. The variation curves of the axial stress increment ($\Delta\sigma$), the axial strain increment (ε), and the pore water pressure ratio (r_u) with the number of loading cycles of the specimen from a depth of 1.6 m are illustrated in Fig. 5.10. As the number of loading cycles increases, the ability to resist loading gradually decreases. Thus, the amplitude of the $\Delta\sigma$ reduces and stabilizes at a relatively low value finally. The amplitude of the ε with an increase in the number of loading cycles. When liquefaction occurs, the strain may develop in a certain direction. The pore water pressure varies with the cyclic loading, and the excess pore water pressure is generated and rises continuously. The effective stress path in this test is illustrated in Fig. 11. The effective stress path presents cyclic mobility behavior in the CTX test. The pore water pressure rapidly increases initially and reaches a stable state in the following cycles.
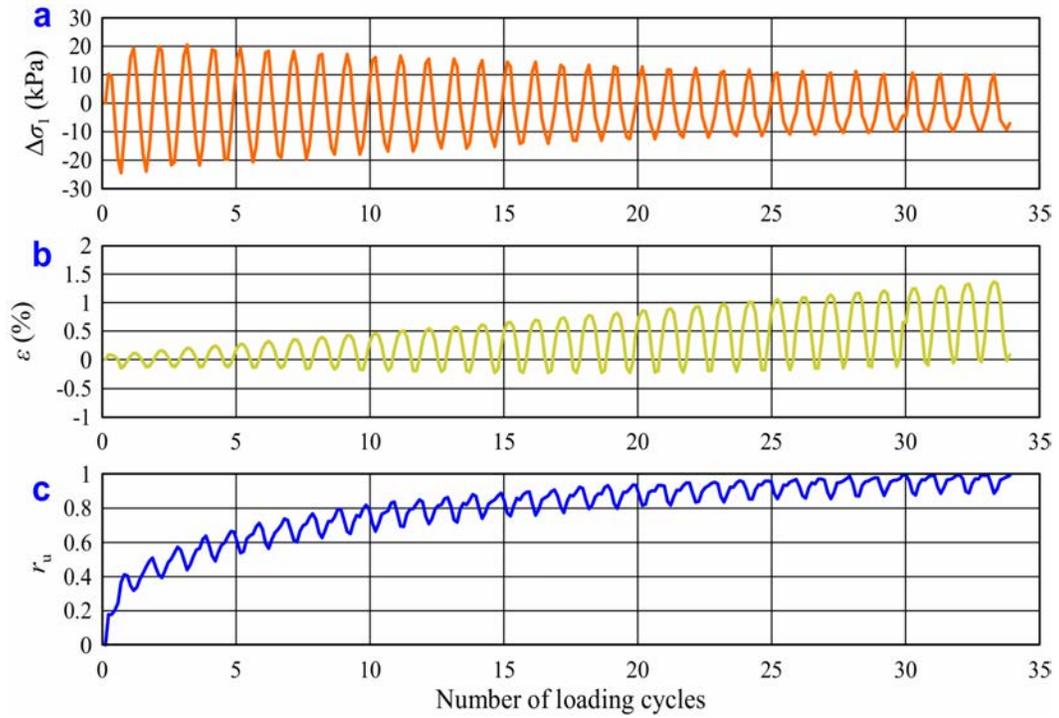
Fig. 5.10 Correlations between the axial stress increment ($\Delta\sigma_1$) (**a**), axial strain increment (ε) (**b**), and pore pressure ratio (r_u) (**c**) with the number of loading cycles for specimens from a depth of 1.6 m in the consolidated-undrained cyclic loading triaxial test
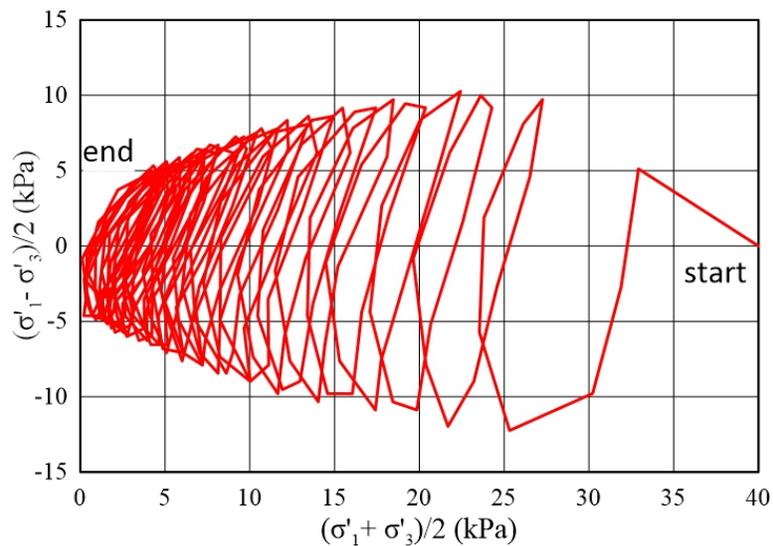
Fig. 5.11 Effective stress path of specimen from a depth of 1.6 m in the consolidated-undrained cyclic loading triaxial test

The relationships between the cyclic shear stress ratio $(\frac{\tau_d}{\sigma_0})$ and the logarithm of N_L ($\lg N_L$) of all specimens are depicted in Fig. 5.12. After a comparison of the liquefaction resistance for the three types of specimens, it is concluded that the liquefaction resistance of the specimen from a depth of 1.9 m is the lowest, and the liquefaction resistance of the specimen from a depth of 2.0 m is the highest. The liquefaction occurred primarily in a depth of 1.9 m, resulting in the overall mobilization of overlapping soil. Thus, the thickness of the sliding mass and the location of the sliding zone are controlled by the low anti-liquefaction strength soil layer with a depth of 1.9 m. The grain size distribution test results reveal that the fine content of the soil layer at a depth of 1.9 m is relatively lower than those of the soil layers at depths of 1.6 m and 2.0 m. Meanwhile, the dry densities of the specimens from the depths of 1.9 m and 1.6 m are almost the same. Thus, it may imply that a proper increase in the fine content for the medium-sandy soil can elevate the anti-liquefaction strength. Compared with the specimen from a depth of 2.0 m, the specimen from a depth of 1.6 m presents a stronger dilation behavior in the static triaxial test but shows a lower anti-liquefaction strength. Therefore, the influence of the dry density on the anti-liquefaction strength is more remarkable, when the soil compositions are similar. Generally, the anti-liquefaction strength of the medium-sandy soil in the Kataragai landslide in lower than that of the pyroclastic fall deposits such as the Iburi landslides. As the groundwater table is high, considerable soil layers were saturated before the 2018 Western-Shimane earthquake. When an earthquake occurred, a high excess pore pressure was generated in the saturated soil, and the shear resistance was further reduced. When the Kataragai landslide occurred, the original structure of the sliding mass cannot be maintained and a disrupted mobilization occurred.
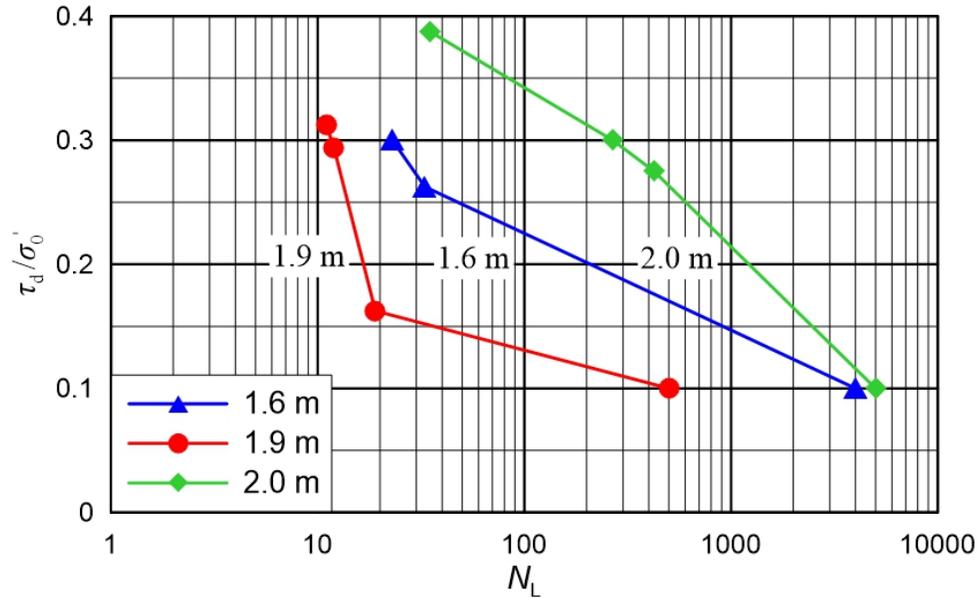
Fig. 5.12 Correlations between the cyclic shear stress ratio $(\frac{\tau_d}{\sigma_0'})$ and the number of cycles required for liquefaction (N_L)

5.4 Seepage flow in the slope

The self-potential test was conducted to locate the seepage flow in the slope, and two sets of the test were carried out along survey lines C-C′ and D-D′. The strikes of both two survey lines are 270°, and the distance between them is 15.0 m. For convenience, the potential of each point in Fig.5.13 is the potential difference between the corresponding point and the base point C. As is revealed in Fig. 5.13, the potential of the points in line C-C′ is higher than the corresponding points in line D-D′. Thus, seepage flows must be existent perpendicular to the survey line. In addition, evident low values appear in the points proximal to pond 1 for both survey lines. It means the flow intensity near pond 1 is stronger than other downstream locations.
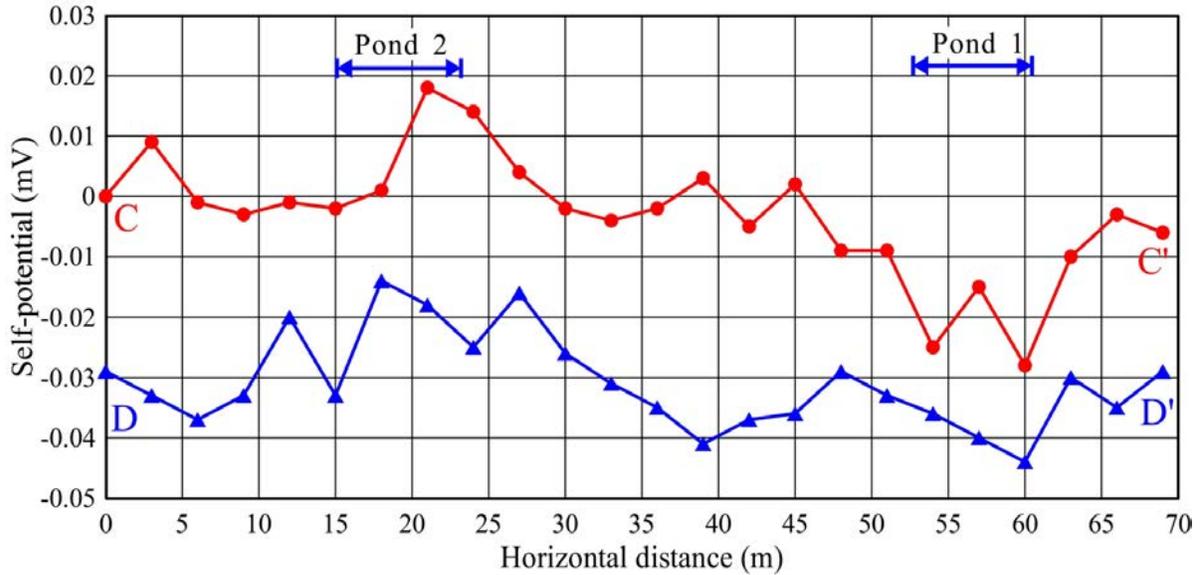
Fig. 5.13 Self-potential test results along survey line C-C′ and D-D′

As a refilled slope, the soil should be relatively homogenous. In the aforementioned study, the occurrence of the Kataragai landslide has been attributed to the existence of the low anti-liquefaction strength soil layer with less fine content and lower dry density. Moreover, the dry density of the soil decreases to a low value and then increases in the vertical direction. Therefore, it can be concluded that the low anti-liquefaction strength soil layer results from the seepage flow in the slope. Pond 1 is located in the middle of the crown (Fig. 5.1) where the flow intensity is relatively strong. This also verifies the influence of the seepage flow on the Kataragai landslide occurrence.

Discussion

In this work, field investigations were performed in detail to investigate the soil composition, sliding zone, and failure mechanism of the coseismic landslides triggered by the 2018 Hokkaido Eastern Iburi Earthquake. Three types of landslides were confirmed, and all three types of landslides shared the same initiation feature, i.e., the global motion of the soil mass along a low anti-liquefaction strength soil layer in the Ta-d pumice. The positive correlation between Iburi landslide distribution and Ta-d pumice thickness was analyzed on the macro scale. These results emphasize the key controlling role of the Ta-d pumice on the occurrence of the Iburi landslides.

In-situ and laboratory tests were conducted to investigate the shear behavior and the anti-liquefaction strength of the pyroclastic fall deposits. The test results indicate that the Ta-d pumice MS with a D50 of 0.3 mm and the Ta-d pumice CS with a low particle strength have lower anti-liquefaction strength than that of other layers. In fact, the Ta-d pumice MS or fragile Ta-d pumice CS were extensively observed in the Ta-d pumice. The existence of the medium sandy or fragile pumice layers heightens the liquefaction potential of the Ta-d pumice and further encourages the landslide risk under intense ground motion. Therefore, it is concluded that the widespread occurrence of the Iburi landslides results from the localized liquefaction of the medium sandy Ta-d pumice MS or fragile Ta-d pumice CS layers in strong earthquakes. In addition, the dilation behavior and strain-hardening observed in Ta-d pumice FG raises the bar for the occurrence of shear failure and liquefaction. The impact of the earthquake on the soil structure of Ta-d pumice FG is small. This enables the maintenance of the overall structure when the landslide occurs, and the integrated sliding appears.

The Ta-d pumice MS is generally located at the bottom of the Ta-d pumice layer or in the middle of two different colors of Ta-d pumice. The difference in pumice color is generally related to the redox environment caused by the relative deposition position with the groundwater table. The Ta-d pumice CS is generally located at the bottom of the Ta-d pumice layer. The stable interbedded paleosol layer was generated between the deposition of the underlying En-a pumice (19–21 ka) and the superjacent Ta-d pumice (8.7–10 ka). The fine-grained paleosol retains low permeability, and the perched groundwater could maintain a certain level above the paleosol layer. Meanwhile, seepage flow could develop in the Ta-d pumice layer, which enhances the soil erosion and weathering of the Ta-d pumice. This explains the extensive existence of the Ta-d pumice MS or fragile Ta-d pumice CS in the landslide distribution area.

A non-negligible fact is few landslides were triggered even though several earthquakes around the study area had occurred prior to the Iburi earthquake. The largest PGA of the historic earthquakes in the vicinity of the 2018 Iburi landslide area was 3.34 m/s^2 in the 2017 M 5.3 earthquake, recorded in the IBUH01 KiK-net station (Fig. 2.1b). None of these historic earthquakes triggered massive slope failures. This means there is a high potential for the substantial occurrence of slope failures in this area when the PGA is larger than 5 m/s^2. The strong ground motion along with the existence of the widely deposited Ta-d medium sandy pumice and Ta-d fragile pumice are conclude as the foremost decisive factors responsible for the destructive Iburi landslides. This study can provide a guideline for future disaster mitigation operations for this area and a reference for similar areas covered by strong-weathered pumice.

Through a succession of field survey, in-situ test, and laboratory test, the topographic and hydraulic conditions, as well as the failure process of the Kataragai landslide, were analyzed in depth. The Kataragai landslide occurred in a refilled slope mainly composed of medium-sandy soil. The CTX tests indicate this soil is characterized by low anti-liquefaction strength. The groundwater table was high before the slope failure, providing a favorable hydraulic condition for liquefaction occurrence under seismic loading. Several ponds were distributed in the slope with perennial water. These ponds are responsible for the widespread seepage flows in the slope. The seepage flows resulted in the erosion of the fine content in the soil, and the weak layer with low anti-liquefaction strength was formed. When an earthquake occurred, shear failure primarily occurred in the low anti-liquefaction strength soil layer (sliding zone), and excess pore pressure

was generated in other layers meanwhile. The location of the low anti-liquefaction strength soil layer controls the thickness of the sliding mass and the location of the sliding zone, and the generation of the excess pore pressure reduces the shear strength of the soil further. The Kataragai landslide initiated as the mobilization of the disrupted sliding mass in the source area, and the mobilization evolved into flow-like sliding after running across the pre-existent scarp and destroying the pond 4 in the travel path.

The Kataragai landslide occurred in the gentle slope distal to area suffered from the most intense ground motion. Therefore, the sliding mass with low anti-liquefaction strength, the high groundwater table, and the erosion of interlayer resulted from the seepage flow, are the key factors controlling the occurrence of the Kataragai landslide. The research on the failure mechanism of the Kataragai landslide in this work will provide a reference for the disaster prevention in refilled slopes. To elevate the seismic stability of slopes, sandy soil with low liquefaction resistance should be prevented when selecting the refiled materials. The increases in fine content and dry density of the soil can promote the anti-liquefaction strength effectively. Moreover, the surface water and groundwater should be drained off in time to degrade the seepage flow and soil erosion.

Through the study on landslides triggered by the Western Shimane earthquake and the Eastern Iburi earthquake, the controlling role of soil on slope failures can be summarized as follows:

1) The distribution of soil with different properties affects the distribution of landslide during earthquakes;
2) The position of the low anti-liquefaction strength soil layer controls the thickness of the sliding mass and location of the sliding zone;
3) The anti-liquefaction strength of the soil located above the sliding zone determines the sliding mass motion with an integrated state or disrupted state.

The controlling role of the groundwater on slope failures is that the weathering and erosion due to the seepage flow can significantly contribute to the formation of the soil layer with low anti-liquefaction strength.

Conclusions

A succession of field investigations, statistical analysis, and laboratory tests were implemented to the Iburi landslides and Kataragai landslide. Based on the longitudinal and vertical stratigraphic sections, the types of the Iburi landslides are classified in detail and the initiation and motion features of different types of landslide are elaborated. Both in-situ tests and laboratory tests were conducted, and the physical properties, shear strength, and anti-liquefaction strength of the soils of the Iburi landslides and Kataragai landslide were analyzed. The weak pumice layers crucial to the initiation of landslides were further confirmed. Correlation analysis between the Iburi landslide distribution and the pyroclastic fall deposit distribution was performed. The self-potential test was carried out to confirm the existence of the seepage at the crown. The coupling effects of the soil properties and the groundwater on the landslides triggered by the Hokkaido Eastern Iburi earthquake and the Western Shimane earthquake were discussed in detail in this work. Detailed conclusions of this work are summarized as follows.

1. All the 5625 coseismic landslides triggered by the Hokkaido Eastern Iburi earthquake, except for two deep-seated landslides, are shallow debris slides. The majority of the shallow debris slides initiate due to the localized liquefaction of the weak sliding zone at Ta-d pumice. Three types of downslope movements—steep debris slide, gentle debris slide, and the mobilization of V-shaped convergent sliding masses—are generated controlled by the geomorphology.

2. Statistical analysis indicates that the occurrence and distribution of the coseismic landslide are highly consistent with the distribution of the Ta-d pumice. The landslide density increases with an increase in the Ta-d2 pumice thickness.

3. The medium sandy Ta-d pumice MS and the fragile Ta-d pumice CS show lower anti-liquefaction strength, and localized liquefaction may occur under intense ground motion. The liquefied zone further develops to the overall displacement of the pyroclastic fall deposits mantled on the liquefied zone. The stable low-permeability paleosol layer underlying the Ta-d pumice enables the seepage flow in the pumice layer and further results in the erosion and weathering of the Ta-d pumice. This explains the extensive existence of the Ta-d pumice MS or fragile Ta-d pumice CS in the landslide distribution area.

4. The area mantled with the weak Ta-d pumice is likely to suffer from massive slope failures when the PGA is larger than 5 m/s^2. This study can provide a guideline for future disaster mitigation operations for this area and a reference for similar areas covered by strong-weathered pumice.

5. The Kataragai landslide occurred in a slope that refilled by medium sandy soil after clay mining. Several ponds were distributed on the slope with a slope angle of approximately 7°. Seepage flows are confirmed in the slope and the area with the strongest flow intensity appears near to pond 1 in the middle of the main scarp. The seepage flow resulted in soil erosion and flushed away the fine content in the soil. A weak layer with small dry density and low fine content was generated.

6. The anti-liquefaction strength of the soils in the Kataragai landslide is relatively low on the whole, and the anti-liquefaction strength of the weaker layer in the sliding zone is lower than other soil layers. Failure firstly occurred in this weak layer when an earthquake occurred and excess pore water pressure was generated in other soil layers as well, reducing the shear resistance of the soil. The original structure of the slope was destroyed and the sliding mass mobilized in a disrupted state. The disrupted sliding mass evolved into flow-like mobilization after running across the pre-existent scarp and destroying the pond in the slope.

7. Since the sandy soil is prone to liquefaction under seismic loading, sandy soil should be refrained when refilling the slope. Moreover, the increases of the fine content and the dry density of the soil can improve the seismic stability of the slope, as the soil with higher fine content and larger dry density has stronger anti-liquefaction strength. Much attention should be paid to the ponds on the slope. The seepage flow resulted from the ponds can reduce the soil strength both by soil erosion and saturation.

8. The position of the weak soil layer commonly controls the thickness of the sliding mass and locality of the sliding zone. Meanwhile, the weathering and erosion due to the seepage flow can significantly contribute to the formation of weak soil layers.

References

Cabinet office (2018) About damage situation on the 2018 Hokkaido Eastern Iburi Earthquake, 29 October 2018, 17:30

Chigira M, Yagi H (2006) Geological and geomorphological characteristics of landslides triggered by the 2004 Mid Niigta prefecture earthquake in Japan. Eng Geol 82(4):202–221. https://doi.org/10.1016/j.enggeo.2005.10.006

China Ministry of Construction (CMC) (2010) Code for Seismic Design of Buildings (GB50011-2010)

Collins BD, Jibson RW (2015) Assessment of existing and potential landslide hazards resulting from the April 25, 2015 Gorkha, Nepal earthquake sequence. U.S. Geological Survey Open File Report 2015–1142, Reston, VA

Corwin RF (1991) Evaluation of effects of cutoff wall construction on seepage flow using self-potential data, east embankment Wells dam. Report for Douglas County Public Utility District No. 1, Washington

Dunning SA, Mitchell WA, Rosser NJ, Petley DN (2007) The Hattian Bala rock avalanche and associated landslides triggered by the Kashmir earthquake of 8 October 2005. Eng Geol 93(3):130–144. https://doi.org/10.1016/j.enggeo.2007.07.003

Faris F, Wang F (2014) Investigation of the initiation mechanism of an earthquake-induced landslide during rainfall: a case study of the Tandikat landslide, West Sumatra, Indonesia. Geoenvironmental Disasters 1(1):4. https://doi.org/10.1186/s40677-014-0004-3

Fukuoka H, Sassa K, Scarascia-Mugnozza G (1997) Distribution of landslides triggered by the 1995 Hyogo-ken Nanbu earthquake and long runout mechanism of the Takarazuka Golf Course landslide. Journal of Physics of the Earth 45(2):83-90

Fukuoka M (1966) Damage to civil engineering structures. Soils and foundations 6(2):45-52. https://doi.org/10.3208/sandf1960.6.2_45

Furukawa R, Nakagawa M (2010) Geological Map of Tarumae Volcano 1:30,000. Geological Map of Volcanoes 15. Geological Survey of Japan, AIST

Geospatial Information Authority of Japan, GSI (2018) Crustal deformation associated with the Western Shimane earthquake occurred at 01:32 on April 9, 2018. https://www.gsi.go.jp/chibankansi/chikakukansi_shimane20180409.html. Accessed 21 April 2018

Geospatial Information Authority of Japan, GSI (2018) The 2018 Hokkaido eastern Iburi earthquake: fault model (preliminary). https://www.gsi.go.jp/cais/topic180912-index-e.html. Accessed 12 October 2018

Gorum T, van Westen CJ, Korup O, van der Meijde M, Fan X, van der Meer FD (2013) Complex rupture mechanism and topography control symmetry of mass-wasting pattern, 2010 Haiti earthquake. Geomorphology 184:127-138. http://dx.doi.org/10.1016/j.geomorph.2012.11.027

Gratchev I, Towhata I (2010) Geotechnical characteristics of volcanic soil from seismically induced Aratozawa landslide, Japan. Landslides 7(4):503-510. https://doi.org/10.1007/s10346-010-0211-2

Harp EL, Jibson RW, Kayen RE, Keefer DK, Sherrod BL, Carver GA, Collins BD, Moss RE, Sitar N (2003) Landslides and liquefaction triggered by the M 7.9 Denali fault earthquake of 3 November 2002. GSA today 13(8):4-10. https://doi.org/10.1130/1052-5173(2003)013%3C0004:LALTBT%3E2.0.CO;2

Huang R, Pei X, Fan X, Zhang F, Li S, Li B (2012) The characteristics and failure mechanism of the largest landslide triggered by the Wenchuan earthquake, May 12, 2008, China. Landslides 9(1):131–142. https://doi.org/10.1007/s10346-011-0276-6

Ishido T, Mizutani H, Baba K (1983). Streaming potential observations, using geothermal wells and in situ electrokinetic coupling coefficients under high temperature. Tectonophysics 91(1-2): 89-104

Ishihara K, Okusa S, Oyagi N, Ischuk A (1990) Liquefaction-induced flow slide in the collapsible loess deposit in Soviet Tajik. Soils and foundations 30(4):73-89. https://doi.org/10.3208/sandf1972.30.4_73

Japan Meteorological Agency (2018a) The 2018 Hokkaido Eastern Iburi Earthquake-Portal-.http://www.jma.go.jp/jma/menu/20180906_iburi_jishin_menu.html. Accessed 12 October 2018

Japan Meteorological Agency (2018b) Technical Description-2 Magnitude Determination. https://www.data.jma.go.jp/svd/eqev/data/nwptac/tech2.html. Accessed 12 October 2018

Japan Meteorological Agency (2018c) Information about the Western Shimane earthquake occurred at 01:32 on April 9, 2018. https://www.jma-net.go.jp/matsue/houdou/2018.04.09-4_oshirase.pdf. Accessed Accessed 21 April 2018

JGS (The Japanese Geotechnical Society) (2010) Soil test: basic and guidance (The second revision). Maruzen press

Katsumata K, Ichiyanagi M, Ohzono M, Aoyama H, Tanaka R, Takada M, Yamaguchi T, Okada K, Takahashi H, Sakai SI, Matsumoto S (2019) The 2018 Hokkaido Eastern Iburi earthquake (M_{JMA} = 6.7) was triggered by a strike-slip faulting in a stepover segment: insights from the aftershock distribution and the focal mechanism solution of the main shock. Earth Planets Space 71:53. https://doi.org/10.1186/s40623-019-1032-8

Keefer DK (1994) The importance of earthquake-induced landslides to long-term slope erosion and slope-failure hazards in seismically active regions. Geomorphology 10:265-284. https://doi.org/10.1016/0169-555X(94)90021-3

Kimura G (1994) The latest Cretaceous-early Paleogene rapid growth of accretionary complex and exhumation of high pressure series metamorphic rocks in northwestern Pacific margin. J Geophys Res Solid Earth 99(B11):22147–22164. https://doi.org/10.1029/94JB00959

Kobayashi T, Hayashi K, Yarai H (2019) Geodetically estimated location and geometry of the fault plane involved in the 2018 Hokkaido Eastern Iburi earthquake. Earth Planets Space 71:62. https://doi.org/10.1186/s40623-019-1042-6

Li GX (2004) Advanced soil mechanics. Tsinghua Press, Beijing

Liao HW, Lee CT (2000) Landslides triggered by the Chi-Chi earthquake. Proceedings of the 21st Asian Conference on Remote Sensing, Taipei 1-2, pp. 383-388.

Liu S (2016) Soil mechanics (fourth edition). China Architecture & Building Press

Lowrie W (2007) Fundamentals of geophysics. Cambridge university press

Moore JR, Boleve A, Sanders JW, Glaser SD (2011) Self-potential investigation of moraine dam seepage. Journal of Applied Geophysics 74(4): 277-286

National Research Institute for Earth Science and Disaster Resilience (2019) NIED K-NET, KiK-net, National Research Institute for Earth Science and Disaster Resilience.

Organization for Cross-regional Coordination of Transmission Operation, Japan (2018) The 1st Evaluation Committee on large scale blackout associated with the 2018 Hokkaido Eastern Iburi Earthquake, reference 4-1, About events from earthquake occurrence to blackout,"

Ortigao JA (1995) Soil mechanics in the light of critical state theories. Balkema, Rotterdam

Osanai N, Yamada T, Hayashi SI, Kastura SY, Furuichi T, Yanai S, Murakami Y, Miyazaki T, Tanioka Y, Takiguchi S, Miyazaki M (2019) Characteristics of landslides caused by the 2018 Hokkaido Eastern Iburi Earthquake. Landslides 16(8):1517-1528. https://doi.org/10.1007/s10346-019-01206-7

Owen LA, Kamp U, Khattak GA, Harp EL, Keefer DK, Bauer MA (2008) Landslides triggered by the 8 October 2005 Kashmir earthquake. Geomorphology 94:1–9. https://doi.org/10.1016/j.geomorph.2007.04.007

Ozaki M, Taku K (2014) 1:200,000 Land geological map in the Ishikari Depression and its surrounding area with explanatory note. Seamless Geoinformation of Coastal Zone

"Southern Coastal Zone of the Ishikari Depression", Seamless Geological Map of Costal Zone S-4, Geological Survey of Japan ALST

Pei X, Zhang X, Guo B, Wang G, Zhang F (2017) Experimental case study of seismically induced loess liquefaction and landslide. Engineering geology 223:23-30. http://dx.doi.org/10.1016/j.enggeo.2017.03.016

Qureshi MU, Towhata I, Yamada S, Aziz M, Aoyama S (2009) Geotechnical risk assessment of highly weathered slops using seismic refraction technique. In: Oka F, Murakami A, Kimoto S (eds) Prediction and simulation methods for geohazard mitigation. Taylor & Francis Group, London

Sassa K (1985) The mechanism of debris flows. In: Proceedings, 11th International Conference on Soil Mechanics and Foundation Engineering, San Francisco, 1:1173–1176

Sassa K, Fukuoka H, Scarascia-Mugnozza G, Evans S (1996) Earthquake-induced-landslides: distribution, motion and mechanisms. Soils Found 36(Special):53–64. https://doi.org/10.3208/sandf.36.Special_53

Sassa K, Fukuoka H, Wang F, Wang G (2005) Dynamic properties of earthquake-induced large-scale rapid landslides within past landslide masses. Landslide 2(2):125–134. https://doi.org/10.1007/s10346-005-0055-3

Scott RF, Zuckerman KA (1972) Sandblows and liquefaction. The Great Alaska earthquake of 1964-engineering publication 1606, National Academy of Sciences, Washington, D.C., 179–189

Seed HB (1968) Landslides during earthquakes due to soil liquefaction. J. Geotech. Engrg. Div. 194(5):1055-1122

Seed HB, Idriss IM, Makdidi F, Nanerjee N (1975) Representation of irregular stress time histories by equivalent uniform stress series in liquefaction analyses. Report No. UCB/EERC-75/29. Earthquake Engineering Research Centre, U.C. Berkeley

Shao X, Ma S, Xu C, Zhang P, Wen B, Tian Y, Zhou Q, Cui Y (2019) Planet Image-Based Inventorying and Machine Learning-Based Susceptibility Mapping for the Landslides Triggered by the 2018 Mw6.6 Tomakomai, Japan Earthquake. Remote Sens 11(8):978. https://doi.org/10.3390/rs11080978

Skempton AW (1954) The Pore-Pressure Coefficients A and B. Geotechnique (4):143–147

Tajika J, Ohtsu S, Inui T (2016) Interior structure and sliding process of landslide body composed of stratified pyroclastic fall deposits at the Apporo 1 archaeological site, southeastern margin of the Ishikari Lowland, Hokkaido, North Japan. J Geol Soc Jpn 122(1):23–35. https://doi.org/10.5575/geosoc.2015.0037

Takahashi H, Kimura R (2019) The 2018 Hokkaido Eastern Iburi Earthquake and its Aftermath. Journal of Disaster Research 14:1-3

Takch AE, Sadrekarimi A, Naggar HE (2016) Cyclic resistance and liquefaction behavior of silt and sandy silt soils. Soil Dyn. Earthq. Eng. 83, 98–109. http://dx.doi.org/10.1016/j.soildyn.2016.01.004

Tamaki M, Kusumoto S, Itoh Y (2010) Formation and deformation processes of late Paleogene sedimentary basins in southern central Hokkaido, Japan: paleomagnetic and numerical modeling approach. Island Arc 19(2):243–258. https://doi.org/10.1111/j.1440-1738.2009.00698.x

Thompson S, Kulessa B, Luckman A (2012) Integrated electrical resistivity tomography (ERT) and self-potential (SP) techniques for assessing hydrological processes within glacial lake moraine dams. Journal of Glaciology 58(211): 849-858

Tokimatsu K, Yoshimi Y, Ariizumi K (1990) Evaluation of liquefaction resistance of sand improved by deep vibratory compaction. Soils and Foundations 30(3):153-158. https://doi.org/10.3208/sandf1972.30.3_153

Wang F, Cheng Q, Highland L, Miyajima M, Wang H, Yan C (2009) Preliminary investigation of some large landslides triggered by the 2008 Wenchuan earthquake, Sichuan Province, China. Landslides 6(1):47–54. https://doi.org/10.1007/s10346-009-0141-z

Wang F, Fan X, Yunus AP, Subramanian SS, Alonso-Rodriguez A, Dai L, Xu Q, Huang R (2019) Coseismic landslides triggered by the 2018 Hokkaido, Japan (Mw 6.6), earthquake: spatial distribution, controlling factors, and possible failure mechanism. Landslides16(8):1551-1566. https://doi.org/10.1007/s10346-019-01187-7

Wang F, Okeke ACU, Kogure T, Sakai T, Hayashi H (2018) Assessing the internal structure of landslide dams subject to possible piping erosion by means of microtremor chain array and self-potential surveys. Engineering Geology 234: 11-26.

Wang F, Wu YH, Yang H, Tanida Y, Kamei A (2015) Preliminary investigation of the 20 August 2014 debris flows triggered by a severe rainstorm in Hiroshima City, Japan. Geoenvironmental Disasters 2(1):17. https://doi.org/10.1186/s40677-015-0025-6

Wang WN, Nakamura H, Tsuchiya S, Chen CC (2002) Distributions of landslides triggered by the Chi-chi Earthquake in Central Taiwan on September 21, 1999. Landslides 38(4):318-326. https://doi.org/10.3313/jls1964.38.4_318

Wiemer G, Moernaut J, Stark N, Kempf P, De Batist M, Pino M, Urrutia R, de Guevara BL, Strasser M, Kopf A (2015) The role of sediment composition and behavior under dynamic loading conditions on slope failure initiation: a study of a subaqueous landslide in earthquake-prone South-Central Chile. INT J EARTH 104(5):1439-1457. https://doi.org/10.1007/s00531-015-1144-8

Xie D (2011). Soil dynamics. Beijing: Higher Education Press

Xu C, Ma S, Tan Z (2018a) Landslides triggered by the 2016 Mj 7.3 Kumamoto, Japan, earthquake. Landslides 15(3):551-564

Xu C, Xu X (2014) Statistical analysis of landslides caused by the Mw 6.9 Yushu, China, earthquake of April 14, 2010. Natural Hazards 72(2):871-893. http://dx.doi.org/10.1007/s11069-014-1038-2

Xu C, Xu X, Shyu JB (2015) Database and spatial distribution of landslides triggered by the Lushan, China Mw 6.6 earthquake of 20 April 2013. Geomorphology 248:77-92. http://dx.doi.org/10.1016/j.geomorph.2015.07.002

Xu L, Coop MR, Zhang M, Wang G (2018b) The mechanics of a saturated silty loess and implications for landslides. Engineering Geology 236:29-42. http://dx.doi.org/10.1016/j.enggeo.2017.02.021

Yamagata K (1994) Tephrochronological study on the Shikotsu and Kuttara volcanoes in southwestern Hokkaido, Japan. J Geogr 103(3):268–285. https://doi.org/10.5026/jgeography.103.268

Yamagishi H, Yamazaki F (2018) Landslides by the 2018 Hokkaido Iburi-Tobu earthquake on September 6. Landslides 15:2521–2524. https://doi.org/10.1007/s10346-018-1092-z

Yang H, Wang F, Miyajima M (2015b) Investigation of shallow landslides triggered by heavy rainfall during typhoon Wipha (2013), Izu Oshima Island, Japan. Geoenvironmental Disasters2(1):15. https://doi.org/10.1186/s40677-015-0023-8

Yang H, Wang F, Vilimek V, Araiba K, Asano S (2015a) Investigation of rainfall-induced shallow landslides on the northeastern rim of Aso caldera, Japan, in July 2012. Geoenvironmental Disasters 2(1):20. https://doi.org/10.1186/s40677-015-0028-3

Yin Y, Wang FW, Sun P (2009) Landslide hazards triggered by the 2008 Wenchuan earthquake, Sichuan, China. Landslides 6(2):139-152

Zhang S, Li R, Wang F, Iio A (2019a) Characteristics of landslides triggered by the 2018 Hokkaido Eastern Iburi earthquake, Northern Japan. Landslides 16(9):1691-1708. https://doi.org/10.1007/s10346-019-01207-6

Zhang S. (2019b). Spatial distribution analysis and three-dimensional seismic slope stability assessment of coseismic landslides--an application to the 2018 Eastern Iburi Earthquake, Hokkaido, Japan--. Doctoral dissertation, Shimane University

Zlender B, Lenart S (2005) Cyclic liquefaction potential of lacustrine carbonate from Julian Alps. Acta Geotechnica Slovenica 1(2):22-31